Doctoral Dissertation
博士論文

A Study of Baseline Compensation System for Stable Operation of Gravitational-wave Telescopes
(重力波望遠鏡の安定稼働のための基線長補償システムの研究)

A Dissertation Submitted for the Degree of Doctor of Philosophy

December 2019
令和元年12月博士 (理学) 申請

Depertment of Physics, Graduate School of Science,
The University of Tokyo
東京大学大学院理学系研究科
物理学専攻

Kouseki Miyo
三代浩世希

Abstract

In 2015, two LIGO detectors had directly detected the gravitational-wave (GW) from the black hole binary merger event, GW150914. In 2017, three detectors, including Virgo detector, had detected the GW from the neutron star merger, GW170817. Moreover, the electromagnetic counterpart was identified by the follow-up observations. The multi-messenger astronomy was established from this time.

GW observation needs a coincidence detection with multiple GW detectors because only a single detector cannot determine the direction of the GW source. If multiple detectors detect the GW, we can estimate the direction from the differences of these detection times. In order to determine the direction, at least three GW detectors are needed. However, the duty cycle of the GW detectors is almost 60 %, and the duty cycle of the multiple detectors is below 50%.

This duty cycle is limited by the unstable operation of GW detectors, which is caused by the seismic disturbance mainly below 1 Hz. While these seismic noises disturb the baseline in this frequency, the current vibration isolation system for GW detectors does not have the isolation performance in this low-frequency seismic noise, because of the insufficient sensitivity of the inertial sensor used in this isolation system.

In this study, the baseline compensation system has been developed. Unlike the current vibration isolation system, this system uses a 1500 m strainmeter installed in parallel KAGRA baseline, which is named geophysics interferometer (GIF). GIF is designed and developed for monitoring the deformation of the baseline directly below 1 Hz with high sensitivity. For this reason, we designed the new system to compensate for the baseline so that KAGRA interferometer would not be affected by low-frequency seismic disturbances.

In this thesis, two main topics are described: the influence of the seismic disturbances to GW detectors and the baseline compensation system to attenuate these disturbances. The design, the performance, and the advantage of this new system are described. Moreover, the implementation and demonstration of this system on KAGRA interferometer are also described. In the test demonstration, the baseline compensation system is installed on the X-arm cavity, which is the most sensitive component in the GW detectors. As a result, the cavity length fluctuation caused by the deformation of the baseline is reduced by -6 dB above 0.01 Hz and by -20 dB below this frequency.

This result would increase the duty cycle of KAGRA interferometer. If this new

vibration isolation system can be installed in other GW detectors, the coincidence duty cycle can also be improved.

Contents

Chapter 1

Background

This chapter introduces the gravitational-wave (GW) and its detection principle and describes an overview of the current GW detectors and problems related to the duty cycle.

In section 1.1, essential properties and sources of the gravitational-wave are described. After that, the detection principle of the GW by using an interferometer is described in section 1.2, and the techniques for improvement of the sensitivity are described in section 1.3. In section 1.4, the overview of the terrestrial interferometric GW detectors is described, and this section raises some problems related to the duty cycle, which are caused by the large-scale current GW detectors. At the end of the chapter, the outline of this thesis is described in section 1.5.

1.1 Gravitational-wave

Gravitational-wave (GW) is a ripple of the space-time, which propagates at the speed of light. GW was predicted by A. Einstein in 1918 and is a result of the general theory of relativity. Because gravity interaction is weak, the direct discovery of GWs has not done by LIGO until 2015.

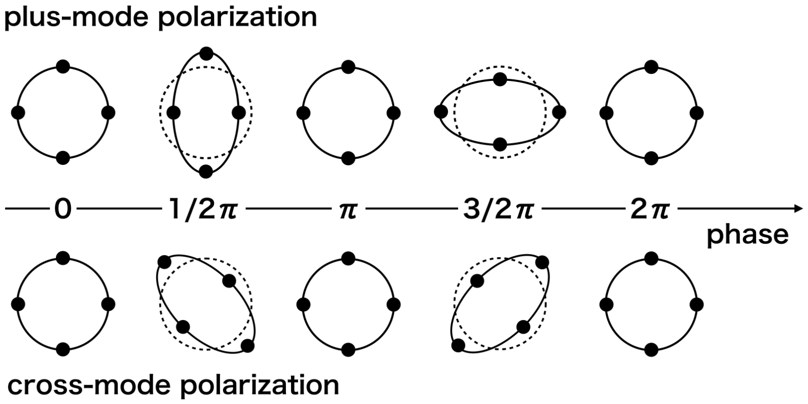

Figure 1.1: Polarizations of the GW propagating in the direction of the paper. These polarizations change the distance as the tidal motion.

1.1.1 Properties of GWs

Two polarized transverse waves

The interval between two events in space-time is described with the metric tensor $g_{\mu\nu}$ as,

$$ds^2 = g_{\mu\nu} dx^\mu dx^\nu (\mu, \nu = 0, 1, 2, 3), \tag{1.1}$$

where dx^μ represents the coordinate distance of the events, and x^μ has 4 components; (ct, x, y, z).

In the general relativity theory[1], the metric tensor $g_{\mu\nu}$ is described by Einstein's equation;

$$R_{\mu\nu}\left(g_{\mu\nu}\right) - \frac{1}{2} g_{\mu\nu} R\left(g_{\mu\nu}\right) = \frac{8\pi G}{c^4} T_{\mu\nu}, \tag{1.2}$$

where $R_{\mu\nu}$ is the Ricci tensor, $R = g^{\mu\nu} R_{\mu\nu}$ is the Ricci scalar curvature, $T_{\mu\nu}$ is the energy-momentum tensor, G is Newton's gravitational constant, and c is the speed of light.

GW is derived from Einstein's equation when the metric can be described as the perturbation $h_{\mu\nu}$ and the Minkowsky space-time $\eta_{\mu\nu}$, thus

$$g_{\mu\nu} = \eta_{\mu\nu} + h_{\mu\nu}. \tag{1.3}$$

In this weak-field regime, Einstein's equation is reduced to a linearized wave-equation whose solution is represented as

$$h_{\mu\nu}(z,t) = \begin{pmatrix} 0 & 0 & 0 & 0 \\ 0 & -h_{+} & h_{\times} & 0 \\ 0 & h_{\times} & h_{+} & 0 \\ 0 & 0 & 0 & 0 \end{pmatrix} \cos\left[\omega\left(\mathrm{t} - \frac{\mathrm{Z}}{\mathrm{c}}\right)\right], \tag{1.4}$$

where ω is the angular frequency of GW, z is the propagation direction of the wave, h_{+} and $h_{\times}$ are the independent polarization of that. Therefore, GW is the transverse wave propagating with the speed of light.

The two polarizations of GW are known as plus and cross polarizations, and these polarizations change the distance between two points, as shown in Figure 1.1.

1.1.2 Sources of Gravitational-wave

In this section, possible astrophysical GW sources are briefly described. More detail studies of the sources can be found in reference [2].

Compact Binary Coalescence

Compact binary coalescence (CBCs), such as black holes and neutron stars, emit a characteristic chirp GW signal. The frequency of a chirp GW signal increase as a function of time. This behavior is caused by losing the angular momentum of the system due to the emission of GW. Advanced LIGO has detected the first GWs from stellar-mass binary black holes (BBHs) in the first observation run (O1), which took place from September 12, 2015, until January 19, 2016. After this observation, Virgo detector joined the Advanced LIGO detectors, and this network has detected the first detection of GWs from a binary neutron star inspiral in the second observation run (O2), which ran from November 30, 2016, to August 25, 2017. Moreover, observation of GWs from a total of seven BBHs [3].

Continuous GWs

Without rotating two objects, asymmetric spinning stars, such as neutron stars and pulsars, could produce detectable GWs, which signal is also well-defined [4, 5].

Burst GWs

In addition to continuous GWs, there are short-duration GWs like a burst event. Supernovae are good candidates to emit te burst GWs [6].

Stochastic GWs

The stochastic background GWs are predicted [7, 8]. This background signal is originated from quantum fluctuations during inflation [9]. Although basically, the stochastic background will appear like random noise in an individual detector, it will be found like a coherent signal in two detectors.

1.2 Interferometric Gravitational-wave detection

The basic design of terrestrial GW detectors is Michelson interferometer [10]. This interferometer is sensitive to the differential length change of its arms, which is changed by the plus mode of the GW, as mentioned in the previous section (section 1.1).

1.2.1 Michelson Interferometer

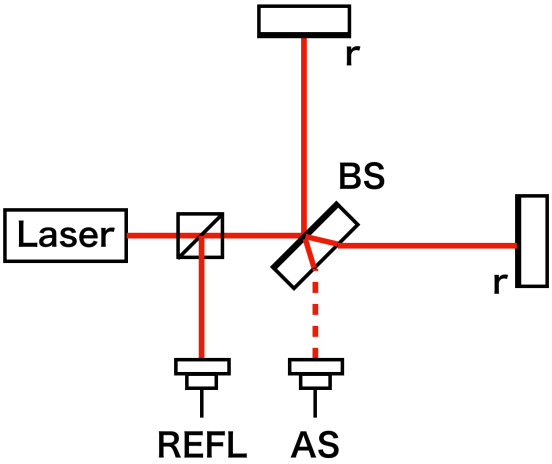

Figure 1.2: Michelson Interferometer.

Michelson interferometer converts from the differential optical phase of two lights, which propagate each arm, to the amplitude modulation of single output light. Consider about the interferometer shown in Figure 1.2. Incident light can be written as,

$$E_{\mathrm{in}} = E_0 e^{i\omega t}, \tag{1.5}$$

where E_0 is the amplitude, and ω_0 is the angular frequency of the laser field. Two lights split by the Beam Splitter (BS) interfere at the Anti-symmetric (AS) port and Reflection (REFL) port. The output field at the AS port is represented as,

$$E_{\mathrm{AS}} = -\frac{1}{2} r E_0 e^{i(\omega_0 t - \phi_x)} + \frac{1}{2} r E_0 e^{i(\omega_0 t - \phi_y)}, \tag{1.6}$$

where r denote the amplitude reflectivity of the end mirrors, and ϕ_x and ϕ_x are the phase delay due to the light traveling in the x and y arms. This output signal can be represented as a single fieled as,

$$E_{\mathrm{AS}} = i r E_0 e^{i(\omega_0 t - (\phi_x + \phi_y)/2)} \sin\left(\frac{\phi_x - \phi_y}{2}\right). \tag{1.7}$$

We find that the amplitude of the output light is a function of the difference between two phases; $\phi_x - \phi_y$. Here, the power of output light at the AS port is obtained by squaring the Eq.(1.7),

$$P_{\mathrm{AS}} \quad = \left[r \sin(\phi_-)\right]^2 P_0 \tag{1.8}$$

Similarly, power of the output light as REFL port is written as,

$$P_{\mathrm{REFL}} \quad = \left[(r \cos(\phi_-))\right]^2 P_0. \tag{1.9}$$

Therefore, we can measure the optical phase difference modulated by GW plus mode as the amplitude changes by using a photo detector (PD).

1.2.2 Static Response

As shown in Eq.(1.4), GW affects as the strain changes. The strain is defined by

$$h = \frac{\Delta L}{L}, \tag{1.10}$$

where L, ΔL are the arm length of the Michelson interferometer and the displacement changes caused by GW respectivly. Bacause the optical phase ϕ_- is given by

$$\phi_- = \frac{4\pi L_-}{\lambda}, \tag{1.11}$$

where L_- is the differential length changes of its arms and λ is the wavelength of the input laser, thus, the strain h is represented as

$$h = \frac{\Delta L_-}{L} = \frac{\lambda}{4\pi L}\Delta\phi_- + \frac{L_-}{L}\left(\frac{\Delta f}{f}\right). \tag{1.12}$$

Moreover, according to Eq.(1.8), because infinitesimal change of the optical phase $\Delta\phi_-$ is given by

$$\Delta\phi_- = \frac{\tan(\phi_-)}{2}\left[\left(\frac{\Delta P_{\mathrm{AS}}}{P_{\mathrm{AS}}}\right) + \left(\frac{\Delta P_0}{P_0}\right)\right], \tag{1.13}$$

where ΔP_0 is the fluctuation of the input laser and ΔP_{AS} is a power fluctuation at AS port, finaly, we get the strain as a function of several fluctuation of physical parameters;

$$h = \frac{\lambda}{8\pi L}\tan(\phi_-)\left[\left(\frac{\Delta P_{\mathrm{AS}}}{P_{\mathrm{AS}}}\right) + \left(\frac{\Delta P_0}{P_0}\right)\right] + \frac{L_-}{L}\left(\frac{\Delta f}{f}\right). \tag{1.14}$$

According to Eq.(1.14), in order to measure the smaller strain changes, one can find that;

- we should expand the baseline length L.
- we should operate the Michelson intereferometer at dark fringe, which means $\phi_- \to 0$ so that the noise contribution from $\Delta P_{\mathrm{AS}}/P_{\mathrm{AS}}$ and $\Delta P_0/P_0$ to the strain h are decreased.
- we should use symmetric arms so that $L_0 \to 0$ in order to decrease the noise contribution from the laser frequency fluctuation $\Delta f/f$.

1.3 Enhancement of the sensitivity

In order increase the sensitivity, current interferometric GW detector use the Dual-Recycled Fabry-Perot Michelson Interferometer (DRFPMI).

1.3.1 Fabry-Perot Michelson Interferometer (FPMI)

According to Eq.(1.10), we need the large-scale interferometer. Fabry-Perot optical cavity enhances the effective arm length of the interferometer.

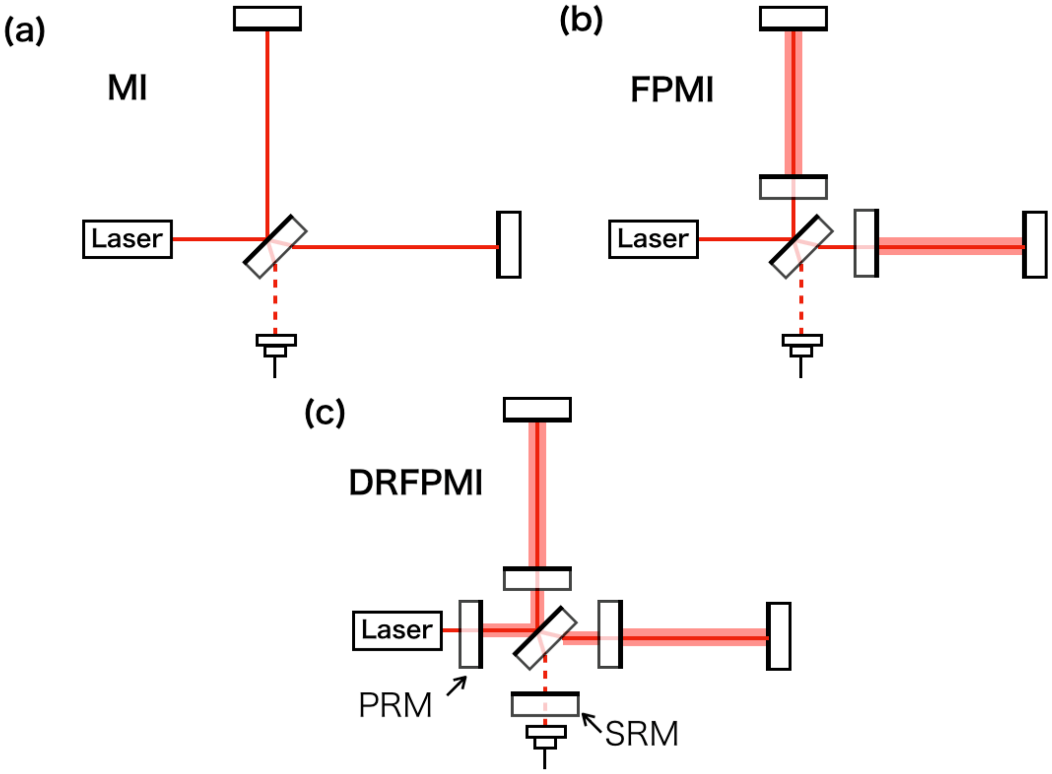

Figure 1.3: Configuration of interferometric GW detector. (a) Michelson interferometer (MI) (b) Michelson interferometer with two Fabry-Perot optical cavities (FPMI). (c) Dual-Recycled FPMI (DRFPMI)

Fabry-Perot Optical Cavity

Fabry-Perot optical cavity increase the effective baseline linegth. Consider the Fabry-Perot optical cavity composed of two mirrors separated by L as shown in Figure 1.4a. In this figure, E_{in}, E_{r}, E_{t}, E are the incident, reflected, and transmitted fields respectively, r_j and t_j are the amplitude reflectivity and transsivity of j-th mirrors ($j = 1, 2$). The averaged bounce number in a Fabry-Perot cavity $\mathcal{N}_{\mathrm{FP}}$ is written as [11]

$$\mathcal{N}_{\mathrm{FP}} = \frac{2\mathcal{F}}{\pi}, \tag{1.15}$$

where $\mathcal{F}$ is a finesse given as

$$\mathcal{F} = \frac{\pi\sqrt{r_1 r_2}}{1 - r_1 r_2}. \tag{1.16}$$

Here, we note that the arm length enhancement can work in case that the cavity length fluctuation is within the linewidth calculated as the full width at half maximum (FWHM);

$$L_{\mathrm{FWHM}} = \frac{\lambda}{2\mathcal{F}}. \tag{1.17}$$

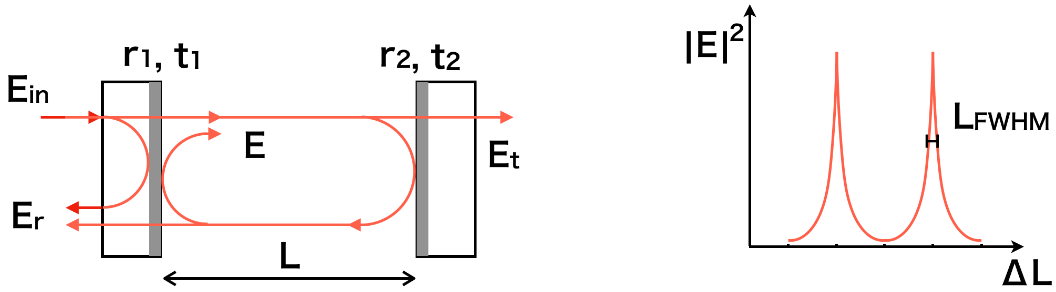

(a) Fabry-Perot optical cavity composed of two mirrors separated by L.

(b) Intra-cavity power as a function of displacement of cavity length.

Figure 1.4: Fabry-Perot optical cavity.

1.3.2 Dual-Recycled FPMI (DRFPMI)

As shown in Figure 1.3(c), the final configuration of the current GW is DRFPMI which has two recycling optical cavity [12].

Power Recycle

In order to decrease shot noise, the power recycling technique is used. In this technique, an additional mirror is installed between the laser and the interferometer to increase the effective laser power by recycling the reflected light from the interferometer. If we increase the laser power, the noise to signal ratio of shot noise decreases as mentioned later.

Signal Recycle

The signal recycling mirror, which is installed on the AS port, is for tunning the frequency band of the GW signal. This mirror enhances the GW signal by recycling the output signal from the interferometer.

1.3.3 Noise

In terms of the interferometric GW detector, noise can be classified into two noises; detection noise and displacement noise of the test mass. The formar noises are, as already described in Eq.(1.14), the detection noise ($\Delta P_{\mathrm{AS}}/P_{\mathrm{AS}}$), the input laser power fluctuation ($\Delta P_0/P_0$), and laser frequency fluctuation ($\Delta f/f$).

Detection noise (Shot Noise)

In an ideal case that the test mass is not disturbed, and as the free mass, the noise of the interferometer is limited by the shot noise.

Shot noise is a noise associated with the fluctuation of the number of photons at the photodetector. In case that the number of photons N is large enough ($N \gg 1$), the number of photons obey the Gaussian distribution with the standard deviation of $\sqrt{N}$. Therefore, if laser power P incidents in the detector, shot noise has a relation with the power;

$$P_{\mathrm{shot}} \propto \sqrt{P} \quad [W/\sqrt{\mathrm{Hz}}]. \tag{1.18}$$

One can find that shot noise is a white noise, which propotional to the square-root of the light power P.

Here, according to Eq.(1.8), the relative error of power at the PD is given by

$$\frac{\Delta P_{\mathrm{AS}}}{P_{\mathrm{AS}}} \propto \frac{1}{\sqrt{P_0}} \quad [1/\sqrt{\mathrm{Hz}}], \tag{1.19}$$

where P_{AS}, ΔP_{AS} are the power at the PD, P_0 is the power of the incident light. This shows that the increased input laser power can decrease the shot noise. For this reason, we increase the input laser power using power recycling mirror.

laser frequency fluctuation

As mentioned in section 1.2.2, symmetric of each arm length is needed to reduce the laser frequency noise. However, because the actual interferometer has an asymmetricity in the arms, the frequency stabilization system is used before inputting the beam to the interferometer. This system is called the input mode cleaner.

laser power fluctuation

The laser power fluctuation also contaminates the sensitivity of the GW detector. The intensity stabilization system (ISS) is used for reducing the noise.

Seismic Noise

Seismic noise is the most trouble displacement noise for interferometric GW detectors. Seismic waves from various excitation sources disturb the test mass through the mechanical structures. Therefore, in order to reduce the seismic noise, the test masses should be suspended by pendulums and kept away from the excitation sources. More details are described in the next chapter.

Newtonian noise

Unlike the seismic noise mentioned above, the Newtonian noise is a noise that the density fluctuation of surrounding objects disturbs the test mass by gravitational interaction [13]. Because this noise propagates through space, it can not be isolated by using vibration isolation. Although the noise does not affect the current 2nd generation GW detectors, it will contaminate the next 3rd generation detectors.

In order to reduce the Newtonian noise, the feedforward control using the seismometer array is proposed [14].

Thermal Noise

In addition to external disturbances such as the seismic origin noise, the mirror substrate, and surface particles caused by the random thermal motion also generate displacement noise. This thermal noise can be classified into two; mirror thermal noise and mirror coating thermal noise [15].

The displacement noise of the mirror thermal noise of the mirror with temperature T is given by [16, 17]

$$G_{\mathrm{SB}}(f) = \frac{4k_BT}{\omega}\frac{1-\sigma^2}{\sqrt{\pi}Ew_0}\phi_{\mathrm{sub}}(f), \tag{1.20}$$

where k_B is a Boltzmann constant, ω is the angular frequency, σ, E, ϕ_{sub} are a Poisson's ratio, Young's modulus, and mechanical loss angle of the bulk of the mirror respectively, and ω_0 is a beam radius. One can find that the mirror thermal noise is decreased by lower temperature or increase the beam radius.

The displacement noise of coating thermal noise is given by [17, 18]

$$G_{\mathrm{CB}}(f) = G_{\mathrm{SB}}(f)\left(1+\frac{2}{\sqrt{\pi}}\frac{1-2\sigma}{1-\sigma}\frac{\phi_{\mathrm{coat}}}{\phi_{\mathrm{sub}}}\frac{d}{w_0}\right), \tag{1.21}$$

were d,ϕ_{coat} are depth and loss angle of the coating.

1.4 Terrestrial Laser Interferometers

A large-scale baseline is the essential feature of interferometric GW detectors to improve the sensitivity.

1.4.1 Overview of detector projects

Various interferometric GW detectors are developed and planed. These detectors are listed table 1.1.

Table 1.1: Terrestrial laser interferometers [19, 20]

generation	project	baseline [m]	geological feature
1st	LISM	20	Granite/gneiss
	CLIO	100	Granite/gneiss
	TAMA	300	Sedimentary soil [21]
	GEO	600	Sedimentary rock
2nd	aLIGO L1	4000	Sedimentary soil
	aLIGO H1	4000	Sedimentary rock
	aVirgo	3000	Sedimentary rock
	KAGRA	3000	Granite/gneiss
3rd	ET	10000	Granite/gneiss (Planning)
	CE	40000	(Under the discussion)

1st Generation

The first generation GW detectors (LISM [22], CLIO [23], TAMA [24], GEO [25]) are small-scale detectors. Although these detectors have performed scientific operations since 1999, no gravitational wave have detected. They demonstrated the working principle of the key technology to increase the sensitivity and constrained the upper limits to several gravitational wave sources [26, 27].

2nd Generation

The second generation GW detectors (KAGRA[28], Advanced Virgo[29], Advanced LIGO[30]) are first large-scale detectors for the enough sensitivity to detect GW signal.

3rd Generation

The third-generation GW detector has a few km-scale detectors. Einstein Telescope (ET) and cosmic explorer (CE) [31] are proposed. It aims to reach a sensitivity about a factor of 10 or more better than the second-generation detectors.

The key features of the third-generation detector are the underground and cryogenic test masses. These are also the features of KAGRA, so KAGRA is also called 2.5 generation detector. Next, we mention LISM and CLIO, which demonstrate the stable GW detector operation and reduction of the thermal noise, respectively.

LISM (first underground GW detector)

LISM, Laser Interferometer gravitational-wave Small observatory in a Mine, is a first GW detector in the underground to demonstrate the stable performance of the detector. The detector of LISM is the Michelson interferometer whose arms contain 20 m Fabry-Perot optical cavities. This arm cavity has a high finesse of 25000. Despite such high finesse, the duty cycle was 99.8 %.

Such a stable operation is owing to the reduction of the baseline length fluctuation of the bedrock. This reduction effect was confirmed on the sensitivity plot of LISM, as shown in Figure 1.5. In this figure, one can find that the sensitivity of the interferometer is less than the noise projection of the horizontal seismic noise below 6 Hz. This reduction was caused by the short-scale baseline because the baseline was moved by the seismic motion as a single object below 6 Hz. This is the reason why LISM performed a stable operation.

CLIO (first cryogenic GW detector)

CLIO, cryogenic laser interferometer observatory, is an interferometer to demonstrate the thermal noise reduction using sapphire mirrors [23]. In order to confirm the reduction, CLIO is also constructed in the underground to attenuate the seismic noise. Moreover, low-vibration pulse tube cryocooler has developed [32]. Owing to these quiet environment, they demonstrated to reduce the sensitivity limited by the thermal noise using a cryogenic test masses [33].

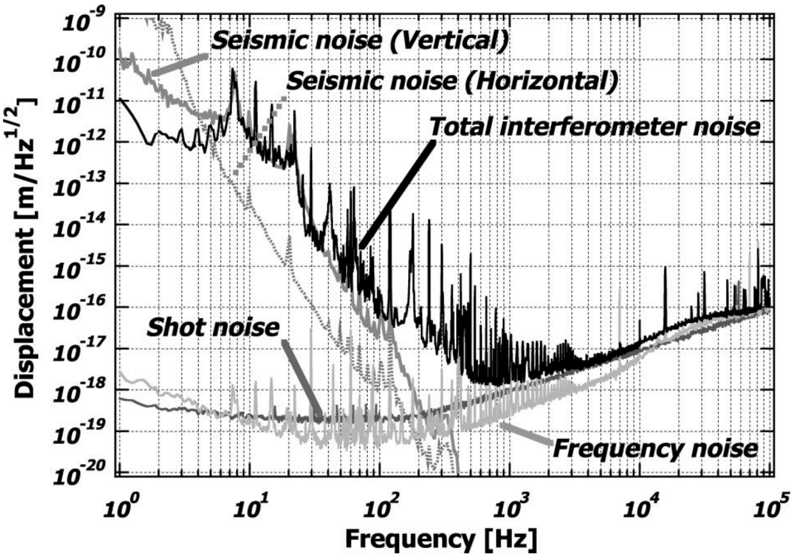

Figure 1.5: The noise equivalent detector sensitivity of LISM. This figure is cited from figure 5 in [22].

1.4.2 Degradation of duty cycle

It is difficult for large-scale GW detectors to keep the long arm cavity on resonance because low-frequency seismic noise disturbs the baseline length.

In the case of the short-scale baseline, the low-frequency seismic noise did not disturb the baseline length because the motion moves the arm cavity as a single object. However, in case the long-scale baseline, the seismic motion below 1 Hz moves the two mirrors of the arm cavity with no correlation. Especially around 0.2 Hz, the amplitude of micro-seisms caused by ocean activities exceeds the linewidth of the arm cavity. This means that the duty cycle of interferometric GW detectors is limited by these low-frequencies.

1.4.3 Improvement of duty cycle

Low-frequency seismic noise potentially cause lock acquisition failure or lock loss.

Arm length stabilization (ALS)

ALS is a technique to reduce the RMS of arm cavity length using frequency-doubled auxiliary lasers before locking the cavity using the main laser [34, 35]. The wavelength of this auxiliary laser is half of the main infrared laser (1064 nm). Thus linewidth is also half according to Eq.(1.17). This means that the auxiliary laser is more easy to lock the arm cavity than the main laser. Therefore, once locking the arm cavity using the auxiliary laser, the ALS system can reduce the RMS of arm cavity length fluctuation using the feedback signal of the auxiliary system so that the main laser can lock the arm cavity. Owing to this system, lock acquisition end within about 10 minutes.

Early earthquake alert

Although the ALS system can bring the interferometer to the observation state in a sufficiently short time, this is used in only the lock acquisition phase, not the observation phase due to the control noise. In the observation phase, we can only use the main laser with narrow linewidth as a sensor for measuring the baseline length. Moreover, we have to use a narrow dynamic range and weak actuator not to contaminate the GW sensitivity with the actuator noise. In this situation, if disturbance will exceed the range of sensors and actuators, the cavity can not keep the locking state.

Actually, the duty cycle of GW detectors is limited by the low-frequency seismic noise in which the vibration isolation system could not attenuate the motion. Especially the long-period earthquake limits the duty cycle [36].

1.5 Outline of thesis

In this thesis, two main topics are described. One is a study of the influence of the low-frequency seismic noise to the large-scale GW detectors. This study shows that the baseline fluctuation is somehow reduced due to a correlated motion at two separated points, and this correlation decrease in the large-scale baseline. For this reason, large-scale GW detectors are suffering from seismic noise. This problem is happening even in the underground. Another topic is the development of the baseline compensation system to reduce residual motion. The feature of this new system is the feedforward control using a strainmeter installed in parallel to the KAGRA baseline, which is named geophysics interferometer (GIF). GIF has been developed for monitoring the deformation of the baseline directly with high sensitivity. The new system compensates for the baseline fluctuation of the arm cavity by using the measurement of GIF strainmeter.

In chapter 2, the properties of the seismic noise are described. The GIF strainmeter's working principle and design are described in chapter 3. After that, the baseline compensation system is described comparing with the current system in chapter 4. In chapter 5, the demonstration of this new system implemented on KAGRA X-arm cavity, and the result is described. At the end of the thesis, chapter 6, conclusion, and future direction are described.

1.6 Summary of the Chapter

In this chapter, the following items are described:

- GW detectors are Michelson interferometer with high finesse optical cavities to enhance the sensitivity.
- Although the large-scale GW detectors improve their sensitivity by longer baseline, the duty cycle of them is degraded because of the long baseline.

Chapter 2

Seismic Noise

Seismic noise causes two issues for laser interferometric gravitational-wave detectors; (1) limitation of the low-frequency sensitivity of the detectors and (2) deterioration of the duty cycle of that. The former problem caused by the seismic noise above 1 Hz, which is associated with an anthropogenic activity. On the other hand, the latter problem caused by the seismic motion below this frequency, which is generated by the natural noise source such as the ocean, disturbs the Fabry-Perot arm cavity to resonate stably.

In order to resolve these issues, a laser interferometer gravitational wave antenna with a baseline length of 20 m (LISM) [22] is constructed underground, because the low-level seismic noise is expected in the underground environment. As a result, the seismic noise in LISM site is less than that in the surface site by two orders of magnitude in 1–100Hz region, and this detector had performed the stable operation with the duty cycle of 99.8%.

However, for km-meter scale GW detector like KAGRA, such a stable operation can not be expected because

- length of the long baseline is susceptible to the low-frequency seismic motion compared with the short one due to a few reduction effect kind of the *common-mode rejection*, and this problem is common in not only all the current detectors but also the next 10 km-scale detectors; Einstein Telescope (ET)[37] and Cosmic Explorer (CE) [31].
- especially in KAGRA site, the microseismic noise correlated with the ocean activity in 0.03–0.3 Hz, which is the most problematic noise for stable operation of GW detector, cannot be reduced even in the underground due to near the sea (40 km from Toyama Bay), and this problem is common in ET which is also will be

constructed in underground but in island [38].

The purpose of this chapter is to describe the above two problems quantitatively. In this chapter, first, section 2.1 gives a theoretical understanding of the seismic noise as the elastic waves. In section 2.2, some general properties of the seismic noise are described by quoting previous researches. Finally, we discuss the problems in section 2.3.

2.1 Theory of seismic waves

Here we introduce characteristics of the seismic wave that will be useful in our later understanding and modeling of seismic effects.

2.1.1 Seismic Waves

The elastrodynamic wave equation without external forces is given by

$$\rho \ddot{\boldsymbol{u}} = (\lambda + 2\mu)\nabla(\nabla \cdot \boldsymbol{u}) - \mu\nabla \times (\nabla \times \boldsymbol{u}), \tag{2.1}$$

where $\boldsymbol{u}$ is the displacement field vetor of the medium, ρ denotes density of the medium, and λ, μ are Lame's first and second parameter.

Body Waves

From Eq.(2.1), we can obtain two characteristic waves; longitudinal wave (primary wave, P-wave) and transverse wave (secondary wave, S-wave). First, using Helmholtz's decomposition, we represent the displacement field vector $\boldsymbol{u}$ as

$$\boldsymbol{u} = \nabla\phi + \nabla \times \boldsymbol{\psi}, \tag{2.2}$$

where ϕ the scalar potential and $\boldsymbol{\psi}$ are the vector potential. Each term of Eq.(2.2) show the divergent and the rotation component of $\boldsymbol{u}$ respectively. Substitute Eq.(2.2) into Eq.(2.1) and after some vector algebra, one can obtain two wave equations;

$$\ddot{\phi} = v_L^2 \nabla^2 \phi, \tag{2.3}$$

$$\ddot{\psi} = v_T^2 \nabla^2 \psi, \tag{2.4}$$

where v_L, v_T are defined as

$$v_L = \sqrt{\frac{\lambda + 2\mu}{\rho}}, \; v_T = \sqrt{\frac{\mu}{\rho}}. \tag{2.5}$$

These phase velocities; v_L, v_T represent that of the P-wave and the S-wave. Show this relationships. Because the scalar potential and the vector potential are obey the wave equation Eq.(2.3) and Eq.(2.4) respectivly, the general solutions of these potentials are given as

$$\begin{aligned} \phi &= \phi_0(\omega t - \boldsymbol{k}\cdot\boldsymbol{x}) && (2.6)\\ \boldsymbol{\psi} &= \boldsymbol{\psi_0}(\omega t - \boldsymbol{k}\cdot\boldsymbol{x}), && (2.7) \end{aligned}$$

where ω, $\boldsymbol{k}$ are the angler frequency and the wave vector. One can obtain the divergent component of displacement filed vector $\boldsymbol{u}$ as

$$\boldsymbol{u}_{\mathrm{div}} = \nabla\phi_0(\omega t - \boldsymbol{k}\cdot\boldsymbol{x}) = -\boldsymbol{k}\phi. \tag{2.8}$$

The displacement of this wave $\boldsymbol{u}_{\mathrm{div}}$ whose phase velocity is v_L propagates along with direction of the wave vector. Therefore v_L is the phase velocity of a longitudinal wave called P-wave. On the other hands, one can obtain the rotation component of $\boldsymbol{u}$ as

$$\boldsymbol{u}_{\mathrm{rot}} = \nabla\times\boldsymbol{\psi_0}(\omega t - \boldsymbol{k}\cdot\boldsymbol{x}) = -\boldsymbol{k}\times\boldsymbol{\psi}. \tag{2.9}$$

This displacement vector $\boldsymbol{u}_{\mathrm{rot}}$ whose phase velocity is v_T is perpendicular to the wave vector. Therefore, v_T is the phase velocity of a transverse wave called S-wave. Furthermore, because λ and μ are positive numbers,

$$v_L > v_T. \tag{2.10}$$

Therefore, the longituginal wave is faster than the transverse wave.

Rayleigh waves

Rayleigh wave is the surface wave and is produced by the interfer of P-wave and S-wave [39]. The phase velocity of the Rayleigh wave given by the equation;

$$\left(\frac{c_R^2}{c_S^2}\right)^3 - 8\left(\frac{c_R^2}{c_S^2}\right)^2 + 8\left(3-\frac{2}{\gamma^2}\right)\left(\frac{c_R^2}{c_S^2}\right) - 16\left(1-\frac{1}{\gamma^2}\right) = 0, \tag{2.11}$$

where c_{R} and c_{S} are the phase velocity of the S-wave and Rayliegh wave, respectively, and $\gamma \equiv c_{\mathrm{P}}/c_{\mathrm{S}}$, where c_{P} is the phase velocity of the P-wave. In case that $0 < (\frac{c_R^2}{c_S^2}) < 1$, the velocity has physically meaningful value. According to Eq.2.11, the ratio $\frac{c_R}{c_S}$ is a function of the ratio of γ. For example, because the phase velocity of P-wave and S-wave are $5.54 \pm 0.05\,\mathrm{km/sec}$ and $3.05 \pm 0.06\,\mathrm{km/sec}$ [40], respectively, the phase velocity of the Rayliegh wave almost $3\,\mathrm{km/sec}$.

2.1.2 Reduction Effect of the Short Baseline

For interferometric gravitational-wave detectors that need a precise length control of the optical resonate cavity, it is appropriate to consider the relative displacement between two points rather than the displacement of a single point.

Differential Motion and Common Motion

We define the motion of two points shown in Figure (2.1) as $\boldsymbol{u}_1 = \boldsymbol{u}(t, \boldsymbol{x}_1)$ and $\boldsymbol{u}_2 = \boldsymbol{u}(t, \boldsymbol{x}_2)$, respectively. The motions of the two points can be represented as the differential motion and the common motion. The displacement of both differential motion and common motion of the two points shown in Figure (2.1) are defined as

$$\boldsymbol{u}_{\mathrm{diff}} \equiv \frac{\boldsymbol{u}_1 - \boldsymbol{u}_2}{\sqrt{2}}, \tag{2.12}$$

$$\boldsymbol{u}_{\mathrm{comm}} \equiv \frac{\boldsymbol{u}_1 + \boldsymbol{u}_2}{\sqrt{2}} \tag{2.13}$$

These two motions defined in Eq.(2.13) and Eq.(2.13) are normalized by $\sqrt{2}$ to conserve the total power.

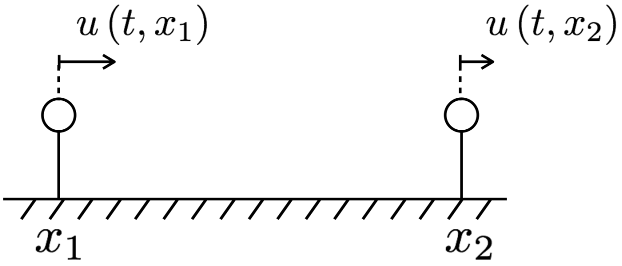

Figure 2.1: The displacements of the two points which are sparated L in X axis. $\boldsymbol{u}(t, \boldsymbol{x})$ is the displacement field vector, where t denotes the time and $\boldsymbol{x}$ denotes the location vector.

Common and Differential Motion Ratio (CDMR)

We define the power ratio of the common motion over the differential motion as common and differential motion ratio (CDMR). This ratio is useful to describe how the differential motion is reduced in the baseline compared to the common motion. CDMR is defined as

$$\mathrm{CDMR} \equiv \sqrt{\frac{\text{Common Motion}}{\text{Differential Motion}}} = \sqrt{\frac{P_{\mathrm{comm}}(\omega)}{P_{\mathrm{diff}}(\omega)}} \tag{2.14}$$

where $P_{\mathrm{comm}}, P_{\mathrm{diff}}$ are the power spectral densities (PSDs) of the differential motion and common motion, respectively. In order to obtain these PSDs, we convert from the autocorrelation function of these. Therefore, first, autocorrelation function C_{diff} of the differential motion is given by its definition in Eq.(2.13)

$$\begin{aligned} C_{\mathrm{diff}}(\tau) &= \frac{1}{2}\left\langle \Big[x_1(t) - x_2(t)\Big]\Big[x_1(t+\tau) - x_2(t+\tau)\Big] \right\rangle & (2.15) \\ &= \frac{1}{2}\Big[C_{11}(\tau) - C_{12}(\tau) - C_{21}(\tau) + C_{22}(\tau)\Big], & (2.16) \end{aligned}$$

,where C_{ij} are the autocorrelation functions of each point and defined as $C_{ij} \equiv \langle x_i(t)x_j(t+\tau)\rangle$, $(i = 1, 2,\ j = 1, 2)$. Here, one can obtain the power spectrum density of differential motion $P_{\mathrm{diff}}(\omega)$ as

$$\begin{aligned} P_{\mathrm{diff}}(\omega) &= \frac{1}{2}\Big[P_1(\omega) + P_2(\omega) - P_{12}(\omega) - P_{12}^*(\omega)\Big] & (2.17) \\ &= \frac{1}{2}\Big[P_1 + P_2 - \mathrm{Re}\,[\gamma] \times 2\sqrt{P_1 P_2}\Big], & (2.18) \end{aligned}$$

where $P_1(\omega), P_2(\omega)$ are the power spectrum densities of each points, and $P_{12}(\omega)$ are the cross spectrum between two point. The parameter γ is the complex coherence between them defined by

$$\gamma \equiv \frac{P_{12}}{\sqrt{P_1 P_2}}. \tag{2.19}$$

Furthermore, assuming that seismic wave propagating each points does not decay, which means $P_1 = P_2 \equiv P$, one can compute the $P_{\mathrm{diff}}(\omega)$ as

$$P_{\mathrm{diff}}(\omega) = P(1 - \mathrm{Re}\,[\gamma]). \tag{2.20}$$

Similarly, the PSD of the common motion can be calculated as

$$P_{\mathrm{comm}}(\omega) = P(1 + \mathrm{Re}\,[\gamma]). \tag{2.21}$$

Finaly, CDMR defined Eq.(2.14) in case the seismic wave does not decay is represented as

$$\mathrm{CDMR} = \sqrt{\frac{1 + \mathrm{Re}\,[\gamma]}{1 - \mathrm{Re}\,[\gamma]}}. \tag{2.22}$$

Eq.(2.22) indicates that CDMR can be expressed by only the coherence γ between of two points. For example, CDMR tends to be larger when γ close to 1. This means that the differential motion is more less than the common motion because the two points move together in the same direction.

Uniform Plane Wave Model

Consider the CDMR when the plane waves are distributed uniformly around the azimuth. Because the coherence in case that the single plane wave propagating with the azimuth angle θ along the direction of arm cavity from x_1 to x_2 in Figure (2.1) is given by

$$\gamma = \exp\left[i\frac{L\mathrm{cos}\theta\omega}{c} \right], \tag{2.23}$$

the coherence in case that the plane waves propagats uniformly is given by the integral of Eq.(2.23) over all direction;

$$\gamma = \frac{1}{2\pi}\int_{-\pi}^{\pi} e^{i\frac{\omega}{c}L\cos\theta} d\theta. \tag{2.24}$$

where the coherence is normized azimuth angle. Therefore, the CDMR is given as

$$\mathrm{CDMR} = \sqrt{\frac{1+J_0(\frac{L\omega}{c})}{1-J_0(\frac{L\omega}{c})}}. \tag{2.25}$$

For later discussion in 2.3.5, the PSD of the differential motion in case of the uniform seismic waves is useful and is given as

$$P_{\mathrm{diff}}(\omega) = P\left[1 - J_0\left(\frac{L\omega}{c}\right)\right]. \tag{2.26}$$

Comparison with different baseline length

The CDMR comparison with LISM, CLIO, KAGRA is shown in Figure 2.2. We assume that the uniform plane wave model with the phase velocity of 3 km/sec. One can find that the km-scale detector has few CDMR below 0.1 Hz than the other short-scale detectors.

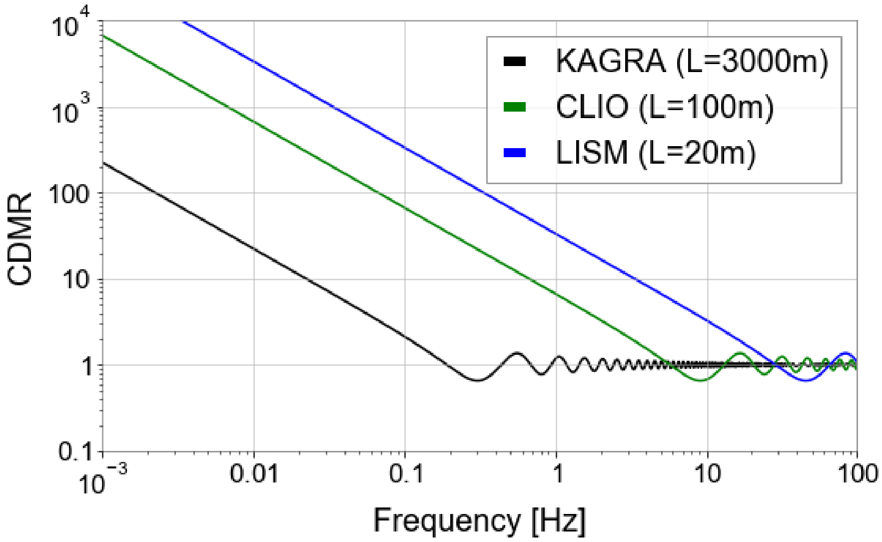

Figure 2.2: CDMR, which is the power ratio of the common motion over the differential motion of baseline in Eq.(2.25), of the underground GW detectors assuming the uniform plane waves model with phase velocity of 3000 m/sec. Black is KAGRA with the 3000 m baseline, green is CLIO with the 100 m baseline, and blue is LISM with the 20 m baseline. The CDMR of the long baseline is worse than that of short baseline.

2.2 Seismic Noise

Characteristics of the seismic noise are related to its origin spatially and temporally. The noise sources are spread anywhere; footsteps, traffic, ocean waves, and these amplitude depends on day-night or weather condition.

As summarized in Table 2.1, the seismic noises above 1 Hz are clearly correlated with cultural activities, and that below this frequency are excited by the natural phenomena [41].

Table 2.1: Two types of seismic noise

Type of noise	Frequency Band	Sources
Cultural Noise	$> 1\,\mathrm{Hz}$	wind, traffic, machinaries, foot steps
Natural Noise	$< 1\,\mathrm{Hz}$	ocean, air pressure, earth tides

This boundary frequency between cultural or natural depends on the soil structure. At the sediment site such as the LIGO [42] and Virgo site [43], the cultural noise can be shifted to a lower frequency and appear below 1 Hz. On the other hand, at the hard rock site such as KAGRA site, the cultural noise can be distinguished from the natural noise for its diurnal variability and apparent only above 1 Hz.

2.2.1 Cultural Noises

The cultural seismic noise contaminates the sensitivity of gravitational-wave detectors in the frequency range of interest for gravitational-waves sources, above 1 Hz. In this frequency band, the cultural noise is dominated by winds or human activities. For example, seismic noise from traffic near the detectors is reported at LIGO site [44], and noise from the vibrations of building excited by winds is reported at Virgo site [45].

2.2.2 Natural Noises

The natural seismic noise affects the stability of the GW detectors below 1 Hz because it deforms the ground on which mounted the detectors.

These natural noises depend on the location. Figure 2.3 shows the noise spectra of the seismic noise measured by Peterson in 75 stations in the world [46]. The NHNM is a spectrum of the average of high background noise power in the stations. Moreover, the primary contributions to NHNM are coastal stations and inland stations on the soft soil. On the other hand, the NLNM represents the seismic noise when microseismic is quiet. Especially, below microseismic, it represents the global seismic noise floor [47].

Microseisms

Microseisms in which the power spectrum has peaked in 50–200 mHz are excited by oceanic waves. These seismic waves can be categorized by the generating mechanism of these [48]. First, the primary ocean microseisms are generated only in shallow waters in coastal regions. In these regions, the water wave energy can be converted directly into seismic energy either through vertical water pressure variations or by the impacts of surf on the shores. There is a correlation between this microseismic peak and the swell at the beaches was known from the data sets studied by [49]. Second, the secondary ocean microseisms could be explained by the superposition of ocean waves of equal period traveling in opposite directions. Therefore, generating standing gravity waves of half the period [50].

The RMS amplitude spectra of both types of the microseisms are strongly depends on the low pressure on the ocean [38].

Seismic Noise Below 20 mHz

Below the microseismic frequency band, the main seismic noise source is an atmospheric pressure change; Rayleigh waves excited by air fluctuation on the surface, and the deformation of the Earth's crust caused by the Newtonian attraction of air mass fluctuation [51, 52]. Fig, 2.4 shows PSDs of the New Low Noise Model (NLNM) [46] and the measured former noise [47]. The noises caused by Rayleigh waves are consistent with the NLNM between 2 Hz and 30 mHz. On the other hand, the noises caused by the Newtonian attraction are increased PSD increases rapidly with decreasing frequency below two mHz.

Earth tides

Below more lower frequency, the earth deformed by tidal forces due to the attraction of the Sun and the Moon in diurnal and semi-diurnal periods [53].

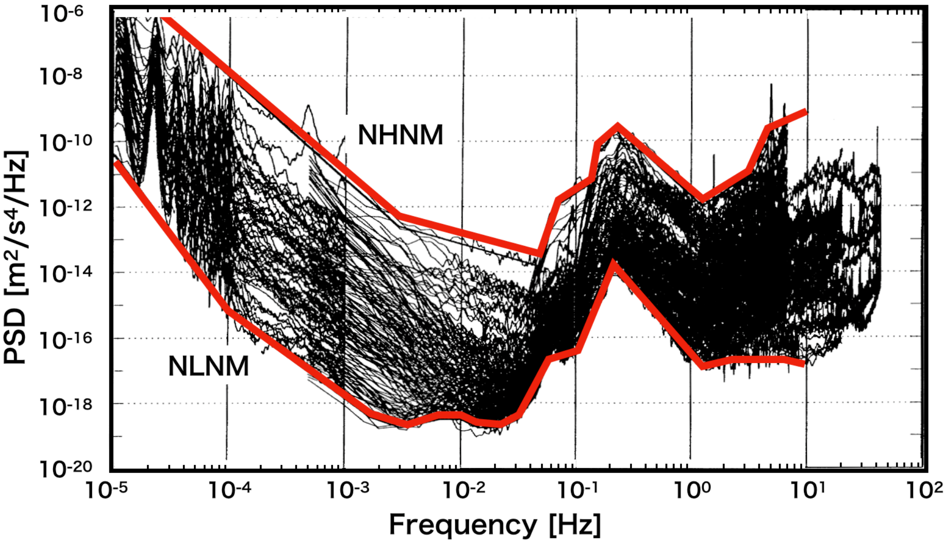

Figure 2.3: PSDs of the seismic noise obtained by Peterson in 75 stations in the world [46]. Each of the black solid lines is PSD divided into 5 different frequency band at the each stations. Each red lines are the new high noise model (NHNM) and the new low noise model (NLNM), respectively.

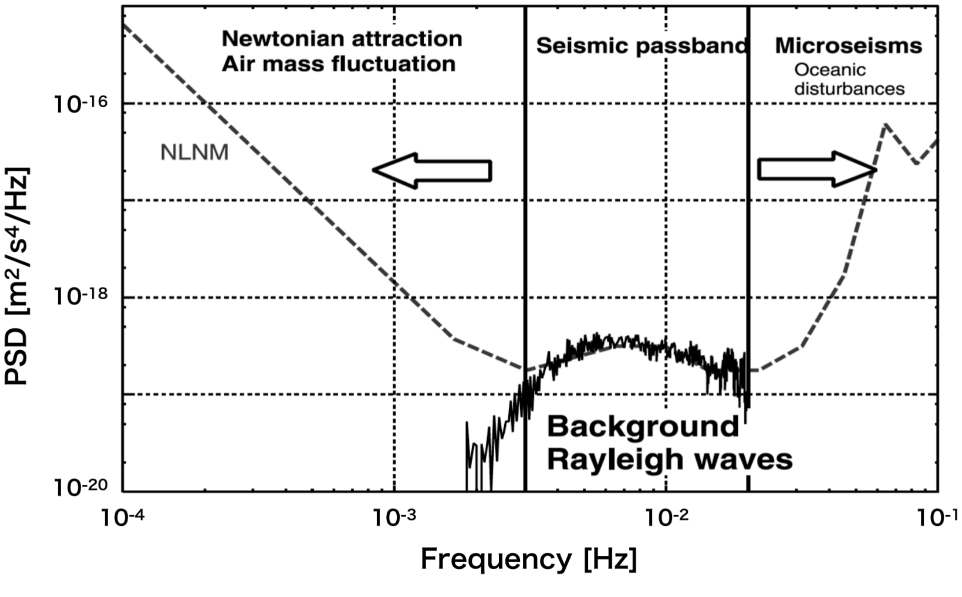

Figure 2.4: Noise contribution below 100 mHz [47].

Large Earthquake in the world

A large magnitude earthquake excites the seismic wave in lower frequency [54, 55]. Although the seismic noise in the observatory depends on both fault and propagation path, here, we assume the same fault. In this situation, it is known that the measurement can be explained by the model (omega-square model);

$$s(\omega) = \frac{S_0}{1 + (\omega/\omega_0)^2}, \tag{2.27}$$

where M_s is the surface magnitude [56], S_0 is a constant propotional to M_s, ω_0 is the corner frequency propotional to $(M_\mathrm{s})^{1/3}$. The spectral of Eq.(2.27)with several surface magnitude are ploted in Figure 2.5. One can find that the large earthquakes trend to be concentrating in lower frequency.

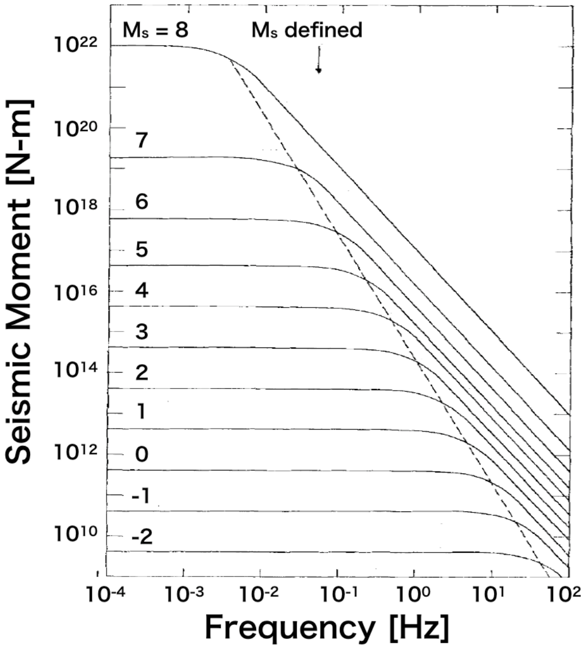

Figure 2.5: omega-square model [55]

2.3 Studies of Seismic Noise of KAGRA Mine

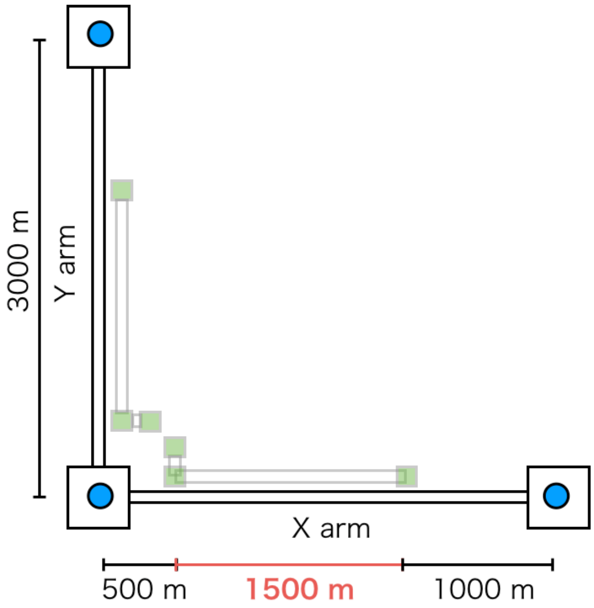

Figure 2.6: Location of the seismometers (blue) and strainmeter (green).

2.3.1 Overview

In KAGRA, we have developed the realtime seismic noise monitor using seismometers. The purpose of this system is to monitor the seismic noise of the ground on which the Type-A suspensions are mounted. We installed the wide-band seismometers (Trillium 120QA) on the second floor of the corner station and each two end stations.

In this section, we have studied the temporal and spatial characteristics of the seismic noises.

2.3.2 Experimental Arrangement

The Trillium 120-QA, which is known as three-component, very broadband, and low-noise seismometer are used. These three outputs are proportional to the ground velocity of two horizontal and one vertical, respectively.

The seismometer is housed in the black thermal insulation cover, as shown in Figure 2.7. Thermal insulation protects two broad categories of thermal couplings that can

Figure 2.7: Trillium 120-QA installed on the second floor at X-end area, which is coverd by black thermal insulation cover

cause unwanted noise [57]. First is the direct coupling to the sensitivity. This coupling typically increases the noise of the vertical channel as a periodic diurnal variation caused by the day-to-night temperature cycle, because the springs that suspended the inertial masses are temperature sensitive. The second is the coupling to tilt from the thermal fluctuation. Tilt converts the vertical acceleration of gravity into horizontal acceleration. This thermally induced tilt noise on the horizontal will be larger than the direct thermal coupling on the vertical channel. To be low sensitivity to both tilt and temperature, this model has a function to center the inertial mass after the initial installation.

The signals of the seismometer are recorded through the data acquisition system developed by LIGO [58]. The analog signal is converted to a digital signal by the 16-bit analog-to-digital converters (ADC) with 16384 Hz sampling. This analog signal is amplified with 30 dB so that the ADC noise does not mask this signal.

2.3.3 Data Processing

The estimation of the amplitude spectrum densities is calculated by the average of 32 segments with 50% overlapping. The single segment has $256\,(2^8)$ sec. The FFT calculation of each segment is done after detrending the linear trend and multiplying the Hanning window.

The error bars of this spectral is calculated by chi-square distribution. For example, the spectrum averaged by 32 obeys the chi-square distribution with 32 degrees of freedom. The confidence interval of $100(1-\alpha)\,\%$ with degrees of freedom ν is given by

$$\frac{\nu \hat{G}(f)}{\chi^2(\nu, 1-\frac{\alpha}{2})} \leq G(f) \leq \frac{\nu \hat{G}(f)}{\chi^2(\nu, \frac{\alpha}{2})}, \tag{2.28}$$

where f is the frequency and $\hat{G}(f)$ is estimator of spectrum. Therefore, the confidence level of 95% is

$$\nu/\chi^2(\nu, 1-\frac{\alpha}{2}) \leq G(f)/\hat{G}(f) \leq \nu/\chi^2(\nu, \frac{\alpha}{2}). \tag{2.29}$$

In case that degrees of freedom is 32, the spectral point lies within 0.65 to 1.75 of the estimates.

2.3.4 Study of Long-term Seismic Noise

Long-term seismic noise is measured by a seismometer installed on the second floor of the X-end area. This area is placed 200 m underground from the surface of the mountain. In comparison to the corner area, human activity in the end area is less because the corner area has parking lots. In comparison to the Y-end area, there is no entrance connected to other mines. Therefore, the X-end area is relatively quiet in the KAGRA mine, regarding the seismic noise induced by human activity.

We estimated the noise spectral using the one-year data, which does not include the glitch noises such as the earthquake or circuit noise. Figure 2.8 shows the amplitude spectrum densities (ASDs) of the horizontal and vertical components of the acceleration.

Below 40 mHz, the horizontal noise is much larger than the vertical noise due to noise arise by temperature fluctuation, and the 10 percentile of vertical noise is close to the NLNM of Peterson. This means that the KAGRA mine is also quiet enough to measure the background seismic noise floor in this band.

From 40 mHz to 1 Hz, in the microseismic noise band, the 10 percentile of both components are middle of the NHNM and NLNM. This indicates that the microseismic in KARGA is not quieter than that in the inland station because the KAGRA site is located on 40 km far from Toyama bay.

Above 1 Hz, both components are close to the NLNM due to the underground environment.

2.3.5 Study of the Differential Motion Reduction

We measured the CDMR described in section 2.1.2 by using the seismometers on the X-end station and corner station.

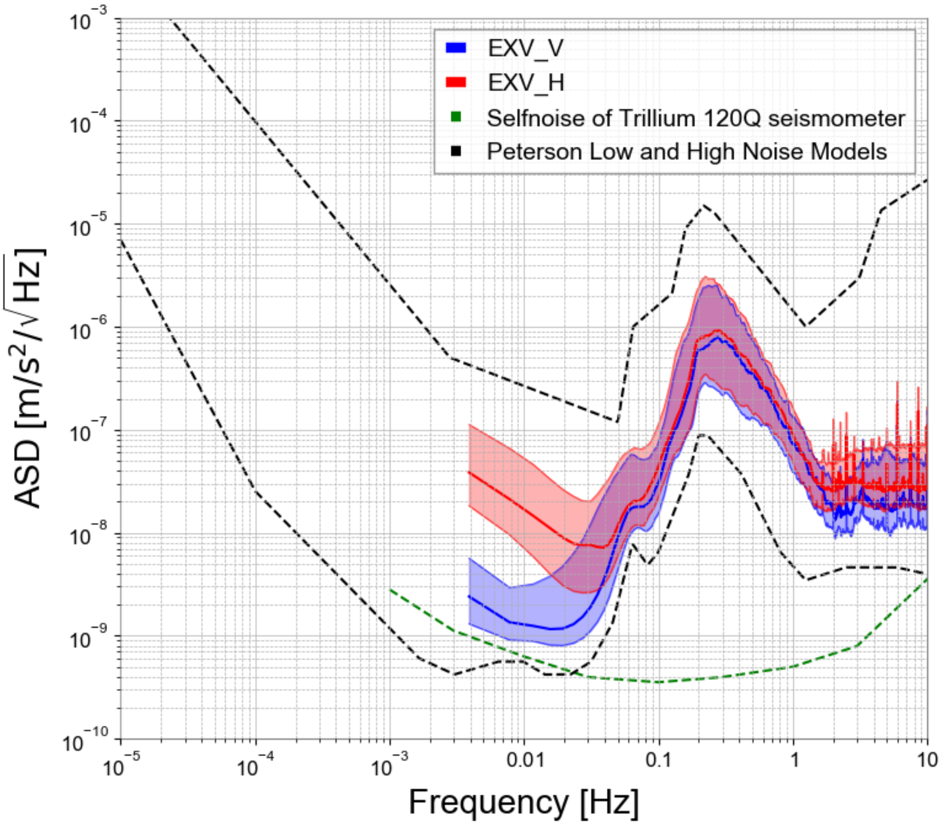

Figure 2.8: The seismic noise in KAGRA mine.

CDMR in X-arm

We calculated the CDMR, which is a ratio of the common motion over the differential motion of the ground given by Eq.(2.14), using two seismometers separated with 3 km a shown in Figure 2.6. The differential and common motion of the X-arm are calculated by the X-axis of each seismometer signal, which is proportional to the ground velocity.

The top of Figure 2.9 shows the common and differential motion of the ground velocity. In this figure, ASDs of the velocity of the differential (solid line) and the common motion (dashed line) are shown. The red and blue indicate the motions of X-arm and Y-arm, respectively. As a reference, the black dashed line shows the self-noise of the Trillium 120Q broadband seismometer multiplied $\sqrt{2}$. Below 0.05 Hz, the ASDs are limited by the noise mentioned in section 2.3.2.

The bottom of Figure 2.9 shows the comparison of the CDMR calculated by these two measured motions, and the CDMR assumed a uniform plane wave model (Bottom).

The measured CDMR is given as red and blue solid lines, which colors indicate the X-arm and Y-arm, respectively. As a reference, the gray line indicates the CDMR assuming the uniform plane waves model in case the phase velocity is in the region from $5 - 3\,\mathrm{km/sec}$, and green dashed line is the CDMR assuming the no correlation between each end point of the baseline. The measured CDMR is consistent with the uniform model in $0.05 - 0.5\,\mathrm{Hz}$. Below this band, the CDMR is close to the no correlation model due to the noise of the seismometers. Below and above this band, the measured CDMR is consistent with the no correlation model.

As a result, the baseline of KAGRA is well modeled with the uniform plane wave model.

2.4 Summary of the Chapter

In this chapter, the following items are described:

- The seismic noise has two origins: cultural or natural. Although the former can be reduced in the underground environment, the latter cannot be. The boundary frequency of these noises is around 1 Hz.
- The km-scale GW detector such as KAGRA is suffering from the low-frequency seismic noise because of the insufficient reduction of the differential baseline motion.

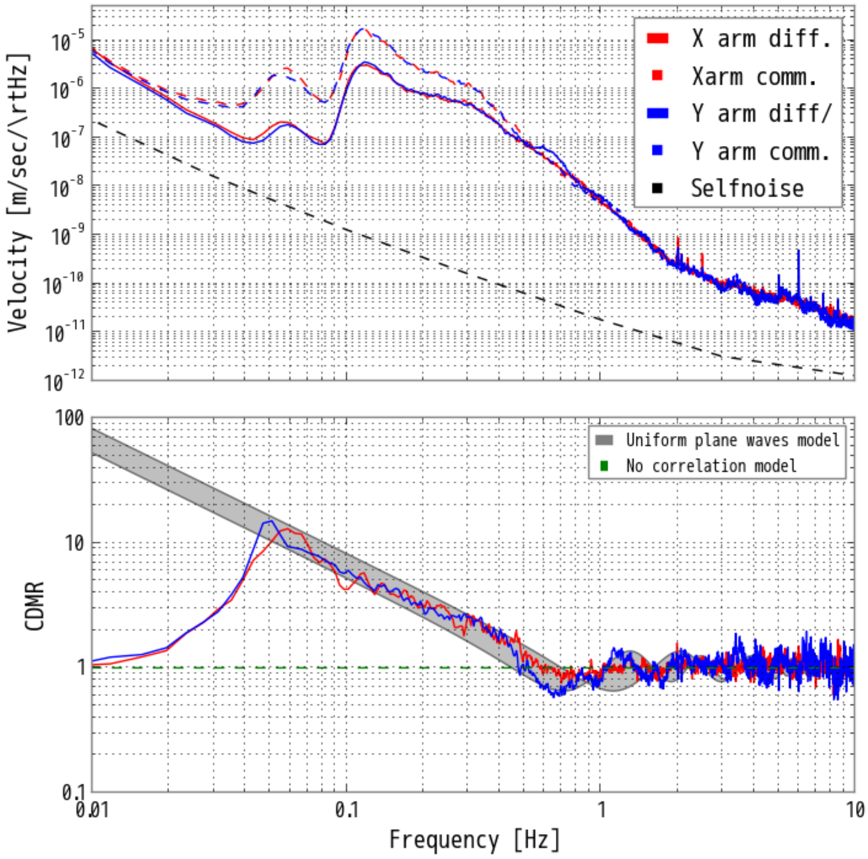

Figure 2.9: Comparison with the measured CDMR and the CDMR assumed the uniform plane waves model.

Chapter 3

Geophysics Interferometer (GIF)

KAGRA is the only GW detector, which has a strainmeter to monitor its baseline length changes. The strainmeter is named Geophysics interferometer (GIF).

GIF is a laser interferometric strainmeter, which is developed by researchers in the Earthquake Research Institute, University of Tokyo. The purpose of the strainmeter is to observe geophysical phenomena: not only earthquakes but also Earth's free oscillations. Unlike a seismometer, the strainmeter has a sensitivity in low-frequency. Moreover, unlike the continuous GPS (CGPS) nets, which also measures a strain ($\sim 10^{-8}$), the strainmeter has more precision ($\sim 10^{-12}$) [59].

In this chapter, instruments of GIF are described. After an overview of GIF in section 3.1, the working principles of the interferometer are described in section 3.2. Optics of GIF is described in section 3.3. Realtime signal acquisition system to send the strain signal to KAGRA is described in 3.4

3.1 Overview

Geophysics interferometer (GIF) is a 1500 m laser strainmeter constructed parallel to the X-arm baseline of KAGRA. As shown in Figure 3.1, GIF is an asymmetric Michelson interferometer, unlike symmetric KAGRA interferometer. Moreover, mirrors of the interferometer of GIF are fixed on the ground in order to monitor the baseline length changes directly. GIF is now only installed on the X-arm, which has been observing the baseline changes for almost three years.

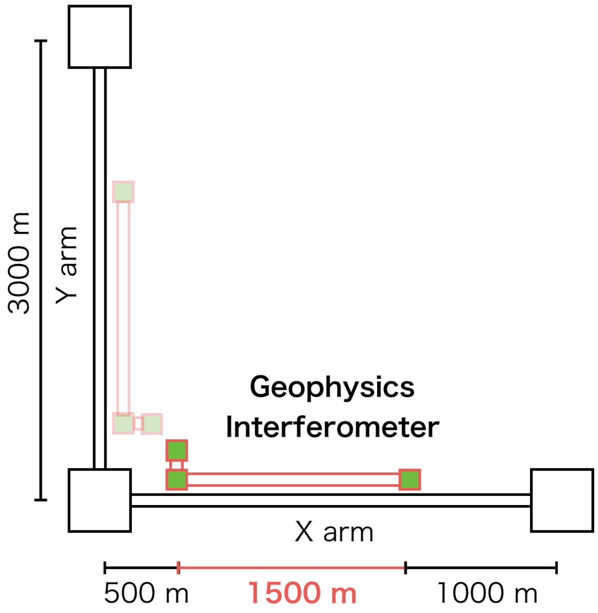

Figure 3.1: Location of geophysics interferometer (GIF). Whereas KAGRA is a symmetric L-shape 3000 m Michelson interferometer, GIF is an asymmetric 1500 m Michelson interferometer. GIF is only installed along the X-arm tunnel.

3.2 Working Principle

As described in section 1.2, the working principle of the strain measurement of GIF is the same as the GW detectors. However, the sensitivity of GIF is limited by the laser frequency noise due to the asymmetric optical configuration.

3.2.1 Asymmetric Michelson Interferometer

A schematic optical layout of the GIF interferometer as an asymmetric Michelson interferometer is shown in Figure 3.2. The asymmetric interferometer measures change of baseline length l_x with reference to the short arm l_y, and its fringe signal is obtained at the REFL port in the case of the GIF.

Here, we consider how the asymmetric arms affect the optical phase of the interferometer. The relation between of the optical phase ϕ_- and the differential of the arms' length $L_- = l_\mathrm{x} - l_\mathrm{y}$ is given as $\phi_- = 4\pi \frac{L_-}{\lambda}$, where λ is the wavelength of the laser. This relation introduces the relation of the infinitesimal changes between in these physical

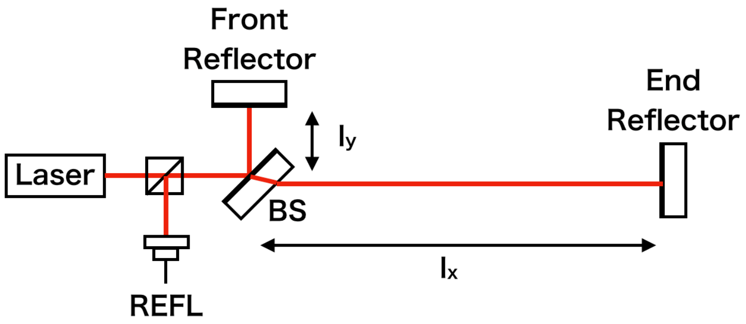

Figure 3.2: Schematic drawing of the GIF as an asymmetric Michelson interferometer, which has two different arm lengths, $l_x \gg l_y$. In this figure, the mode-matching optics and the optics for signal detection are not drawn.

parameters;

$$|\Delta\phi_-| = \frac{4\pi L_-}{\lambda}\left(\left|\frac{\Delta L_-}{L_-}\right| + \left|\frac{\Delta f}{f}\right|\right), \tag{3.1}$$

where Δ denote the infinitesimal change of the parameters and f if the frequency of the laser, and relation $|\frac{\Delta\lambda}{\lambda}| = |\frac{\Delta f}{f}|$ was used to represent with the frequency fluctuation. Assuming enough asymmetricity of each arm length $l_\mathrm{x} \gg l_\mathrm{y}$ and the short reference arm is the rigid bar $\Delta l_\mathrm{y} \ll 1$ (this assumption is true because the short arm of l_y is made of the super-invar plate whose coefficient of thermal expansion is extremely low), Eq.(3.1) can be represented as

$$|\Delta\phi_-| = \frac{4\pi l_\mathrm{x}}{\lambda}\left(|h| + \left|\frac{\Delta f}{f}\right|\right), \tag{3.2}$$

where $h = \Delta l_x / l_x$ is the strain of the baseline. It is clear that the strain and the laser frequency fluctuation are the same response to the optical phase. In other words, the frequency noise directly affects to noise of the strain measurement.

3.2.2 Seismic Strain Response

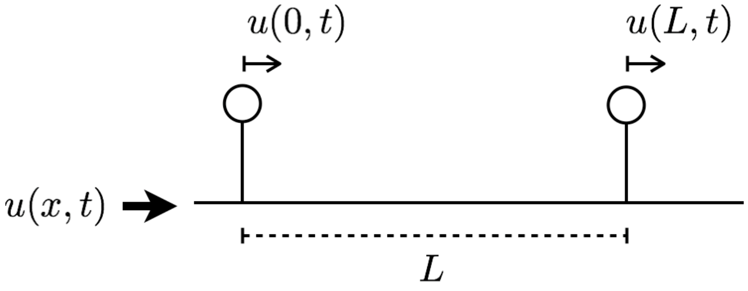

Figure 3.3

Here, we consider the response from strain to the optical phase in the case that the plane seismic waves whose displacement $u(t,x)$ is represented as $u(t,x) = u_0 e^{i(\omega t - kx)}$ with angular frequency of ω and the wavenumber of k. The seismic wave propagates along with the direction of the baseline of the strainmeter (right direction in this figure).

Response from u to ΔL, (H_{disp})

Before calculating the strain response, we calculate the response from the displacement of the seismic wave to the baseline length change. First, because the length fluctuation between two mirrors separated with L can be expressed as

$$\begin{aligned} \Delta L(t) &\equiv u(t,0) - u(t,L) && (3.3)\\ &= u(t,0) - u(t-\tau,0), && (3.4) \end{aligned}$$

where $\tau = L/v$ is the time delay, the transfer function from the displacement to the length fluctuation is given by Laplace transform as

$$H_{\mathrm{disp}}(s) \equiv \frac{\Delta L(s)}{u(s)} = \frac{u(s)\left[1 - \exp(-\tau s)\right]}{u(s)} = 1 - \exp(-\tau s) \tag{3.5}$$

Response from ϵ to ϕ_{-}, (H_{strain})

Because the strain amplitude $\epsilon(x,t)$ is defined as $\epsilon(x,t) \equiv \frac{du}{dx}$, the seismic strain is represented as

$$\epsilon(x,t) \equiv \frac{du}{dx} = \frac{du}{dt}\frac{1}{v} = \frac{s}{v}u(s) \tag{3.6}$$

Therefore, the transfer function from the seismic strain to the displacement is given as

$$\frac{\Delta L(s)}{\epsilon(s)} = H_{\mathrm{disp}} \frac{v}{s} \tag{3.7}$$

Finally, because the transfer function from the length change of the baseline to the optical phase is given as $4\pi/\lambda_{\mathrm{opt}}$, the transfer function from the seismic strain to the optical phase is represented as

$$H_{\mathrm{strain}}(s) = 4\pi \frac{1}{\lambda_{\mathrm{opt}}} \left[1 - \exp(-\tau s)\right] \frac{v}{s}. \tag{3.8}$$

Here, as a summary of these transfer functions, these are related to each other, as shown in figure (3.4).

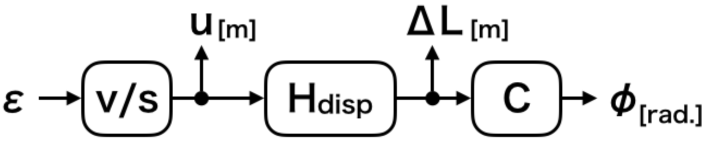

Figure 3.4: The response from seismic strain to optical phase.

Improvement of the sensitivity with longer baseline

Here, we describe the length dependence of the strain response given by Eq.(3.8). The bode plot of the strain response with two different baseline lengths is shown in Figure 3.5, in the case that the phase velocity is 5.5 km. One can find that the DC gain is greater for $L = 3000\,\mathrm{m}$ than the gain for $L = 3000\,\mathrm{m}$, and the corner frequency is lower in the case of long baseline.

Because the corner frequency $f_0 \equiv 1/\tau$ is given as

$$f_0 = \frac{v}{L}, \tag{3.9}$$

if the baseline length is twice, this frequency became a half value, which means a decrease of the observation frequency band. For example, in the case of $L = 1500\,\mathrm{m}$, and assuming the phase velocity of 5.5km/sec, the corner frequency is $f_0 \sim 3.7\,\mathrm{Hz}$. Below this frequency, therefore, the GIF interferometer responses to the strain as the flat response.

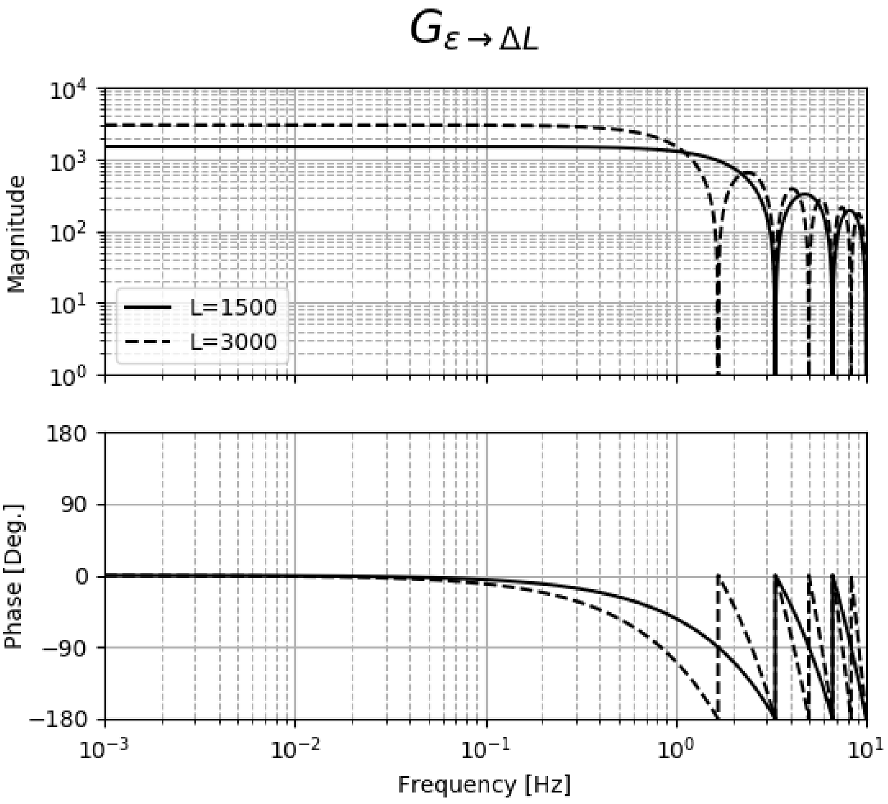

Figure 3.5: Compasison of the transfer function from strain of the baseline ϵ to the length change of that ΔL in the different baseline length.

3.2.3 Noise

Frequency Noise

As mentioned above, the noise of asymmetric interferometer is limited by the frequency noise because the common mode rejection was not worked sufficiently. The GIF, therefore, uses the frequency stabilized laser by using the iodine-absorption line [60]. The fluctuation $\Delta f/f$, which corresponds to the stain, is

$$h = \frac{\Delta f}{f} \sim 7 \times 10^{-13} [1/\mathrm{Hz}]. \tag{3.10}$$

Residual Gas Noise

Bcause residual gas fluctuates the optical path, length measured by interferometer is also fluctuates. The opttical path L_{opt} is given by $L_{\mathrm{opt}} = nL$, where L is the length of the baseline and n is the refraction index in the optical path relative to the path in the vacuum. Under the pressure of p in vacuum, the index n is approximated as $n = 1 + c_0(p/p_0)$, where c_0 denotes the relattive refractive index, p_0 is pressure in standard air at 1 atm. The apparent strain due to the residual pressure is given as [61];

$$h = (L_{\mathrm{opt}} - L)/L = c_0(p/p_0) \sim 3 \times 10^{-9} p. \tag{3.11}$$

In order to maintain the strain sensitivity; 3×10^{-13}, the vacuum pressure should be below 1×10^{-4} [Pa]. However, actual vacuum pressure is 1×10^{-2} [Pa], then strain is $\sim \times 10^{-12}$.

3.3 Optics

In the previous discussion, the laser light was implicitly assumed the plane wave, which does not change the optical phase and radius of the beam when it propagates, but the actual beam is not. The actual beam requires a design of these beam profiles to interfere with the beam within a finite scale. In this section, we assume a Gaussian beam and describe the design for the GIF interferometer.

3.3.1 Gaussian Beam

Gaussian beam

Ideal Gaussian beam has the fundamental spatial mode called TEM_{00}. The whose electric field of the beam propagating to z axis is given by [62, 63]

$$u(x,y,z) = \sqrt{\frac{2}{\pi w^2(z)}}\exp\left(i\zeta(z) - \mathrm{i}k\frac{x^2+y^2}{2R(z)} - i\frac{2\pi}{\lambda}z\right)\exp\left(-\frac{x^2+y^2}{w^2(z)}\right), \tag{3.12}$$

where λ, w_0 are the wavelength and the beam radius at $x=0$ of the beam. In addition,

$$z_0 = \frac{\pi w_0^2}{\lambda} \tag{3.13}$$

$$w(z) = w_0\sqrt{1+\left(\frac{z}{z_0}\right)^2}, \tag{3.14}$$

$$R(z) = z\left[1+\left(\frac{z_0}{z}\right)^2\right], \tag{3.15}$$

$$\phi(z) = \arctan\left(\frac{z}{z_0}\right) \tag{3.16}$$

are Reyliegh range and radius, curvature, and Gouy phase of the beam as a function of z, respectively. One can find that power of the beam $|u^2|$ has a Gaussian distribution as shown in Figure 3.6a according to Eq.(3.12).

Beam profiles

As shown in Figure 3.6b, the beam profiles given by Eq.(3.15,3.16,3.16) are plotted as a function of z. In near-field ($z=0$), the beam can be regarded as the plane wave because the beam radius is smallest (beam waist), and the Gouy phase is 0. On the other hand, in far-field, the beam looks like a point source from far distant, and it is regarded as the spherical wave.

3.3.2 Reflector Design

In order to minimize the size of the reflectors, the beam of the GIF interferometer is designed so that the beam waist is in the end reflector, as shown in Figure 3.7. In this case, if the beam waist w_0 is focused at the end reflector, the beam radius at the front

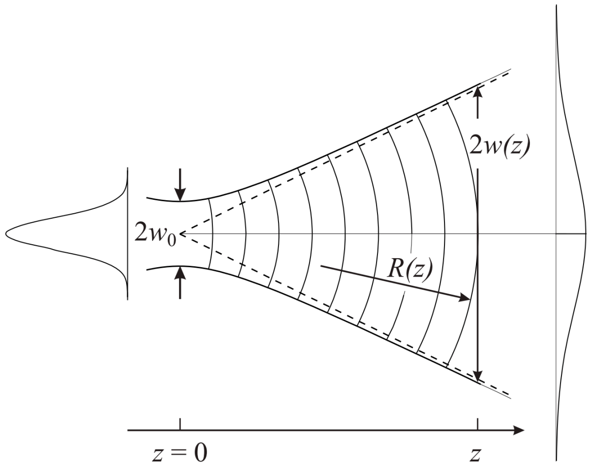

(a) Evolution of a Gaussian beam propagating along the z-axis[64]
w_0 denotes a beam radius at beam weist, where $z = 0$. $w(z)$ and $R(z)$ are the beam radius and curvature at z. Gouy phase is not shown in here.

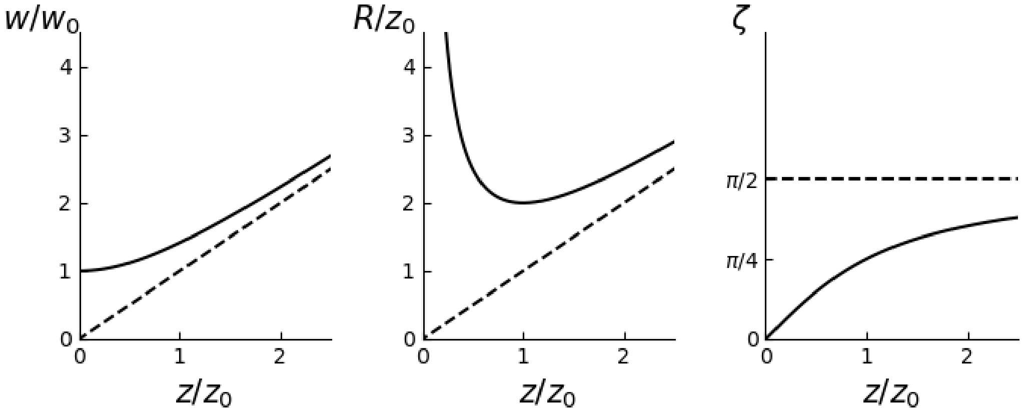

(b) Beam prifile
(left) Beam radius normalized by w_0 as a function of z/z_0, where z_0 is Rayleigh length. (Middle) Beam curvature normalized by z_0. (right) Gouy phase.

Figure 3.6: Gaussian beam.

reflector $w(L)$, which locates 1500 meters from the end reflector, spreads. Therefore, we need to design the beam so that

$$\arg\min_{w_0}\left[w_0 \times \frac{w(L)}{w_0}\right]. \tag{3.17}$$

Substituting Eq.(3.15) into Eq.(3.17), one can obtain the beam waist radius

$$w_0 = \sqrt{\frac{L\lambda}{\pi}} \tag{3.18}$$

We note that the Rayleigh range is $z_0 = L$ in the case of that.

According to Eq.(3.18), the beam waist radius of the GIF is

$$w_0 = \sqrt{1500\,[\mathrm{m}] \times 532\ [\mathrm{nm}]/\pi} = 16\,\mathrm{mm}. \tag{3.19}$$

Furthermore, the beam radius at the front reflector is $w(1500) = \sqrt{2}w_0$. Finally, we determin the size od the reflectors as the three times of the $w(1500)$, then the mininum size of the reflector is $2 \times 3 \times \sqrt{2}w_0 \sim 270\,\mathrm{mm}$.

3.3.3 Input Output Optics

Input-output optics is used for matching the beam profile of the input laser and the interferometer in order to interfere, as shown in Figure 3.7. The output beam from the laser incident to a beam splitter (BS) using (1) a collimator, (2) steering mirror, and (3) concave mirrors in order to be the beam waist at the end reflector. The reflected beams from each reflector are re-combine at Point B, and this interfered light is incidents to the photodetector through another concave mirror and collimator. The mode matching is described in reference [65].

3.3.4 Core Optics

The core optics of the Michelson interferometer are composed of two reflectors and a beam splitter (BS).

3.3.5 Frequency Stabilized Laser

As mentioned in 3.2.3, because the frequency noise of the laser limits the sensitivity of the strain measurement, the GIF interferometer uses the frequency stabilized laser utilizing

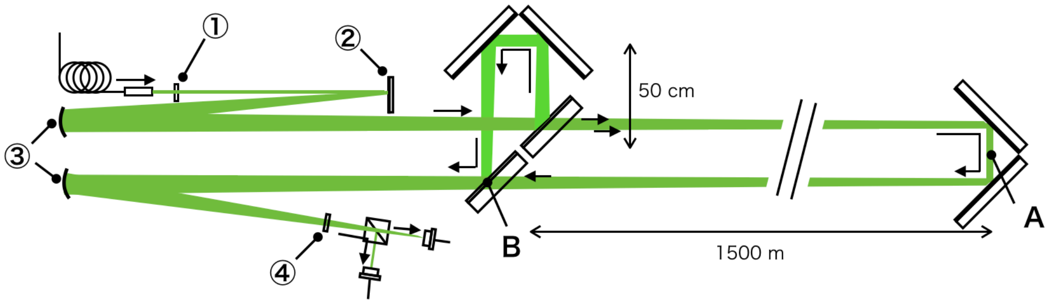

Figure 3.7: Schematic optics layout

(1) A collimator lens for input beam. (2) A flat mirror for steering mirror. (3) Two concave mirrors with a radius of curvature of 9.8 m for mode matching. (4) A collimator lens for output beam. The waist of the beam is at the end reflector at point A. Two reflected on the reflectors are combined at point B.

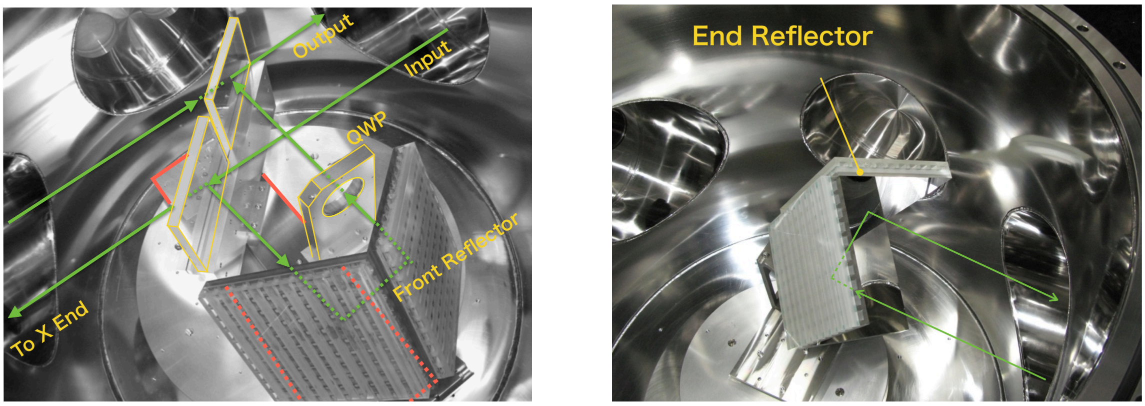

(a) Core optics in the front vacuum chamber. **(b)** Core optics in the end vacuum chamber.

Figure 3.8: The picture of the core optics.

the iodine absorption line [66]. The control diagram of the frequency stabilization system is shown in Figure 3.9. This control is a feedback system in order to reduce the error signal of the laser frequency and the frequency of the iodine absorption line. The error signal is obtained by the PDH method from the absorption signal that is a doppler free signal by using the pump and probe light [67].

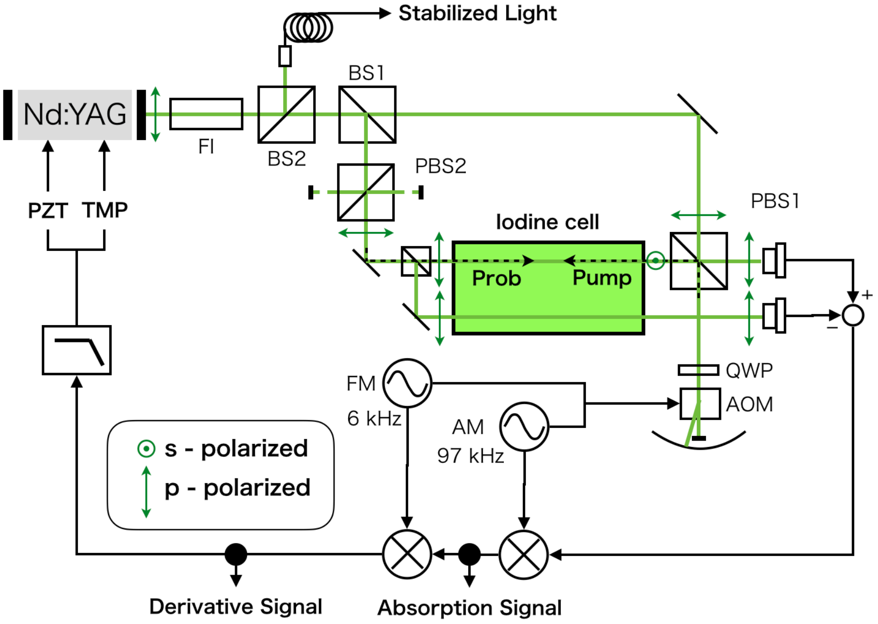

Figure 3.9: Schematic diagram of the frequency-stabilization system of the GIF main laser.

3.4 Realtime Data Aquisition System

Essentially, the GIF is an independent instrument from the KAGRA not to interfere with each other. Therefore, the data acquisition system of each was developed independently. However, in order to use the GIF strainmeter for the baseline compensation system, we need to implement the GIF system into the KAGRA system.

In this section, the realtime data acquisition system is described. In section 3.4.1, we describe the quadrature-phase detection scheme for obtaining the optical phase proportional to the strain on the X-arm baseline. In this scheme, we need the ellipse fitting to obtain the optical phase. In section 3.4.2, the realtime data acquisition system is described. This system process the fitting below 1 msec.

3.4.1 Quadrature Phase Fringe Detection

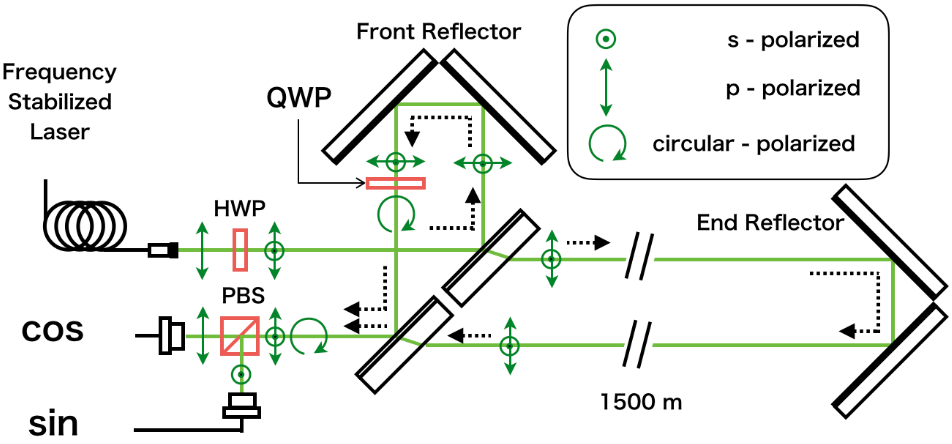

Figure 3.10: Quadrature interferometer used in the GIF strainmeter.

We use the quadrature-phase fringe detection to measure the length change of the baseline with a wide dynamic range [68]. The optical layout for the detection is shown in Figure 3.10. A half-wave plate (HWP) produces a p-polarization and s-polarization. A quarter-wave plate (QWP) delay the optical phase of the s-polarized light with 90 degrees against the other. As a result, one can obtain the quadrature-phase fringes.

The quadrature-phase fringes are detected by two photodetectors, these can be represented as

$$x(t) = x_0 + b\cos(\phi(t)), \tag{3.20}$$

$$y(t) = y_0 + a\sin(\phi(t) + \delta), \tag{3.21}$$

where x and y are the two voltage outputs from the detectors, a and b are the amplitudes of these fringe signals, x_0 and y_0 are the offsets, ϕ is optical phase, and δ is the phase offsets from imperfections [69]. Here, the optical phase ϕ is given by

$$\phi = \arctan\frac{\bar{Y}}{\bar{x}} \tag{3.22}$$

where

$$\bar{Y} = \left(\frac{\bar{y} - \bar{x}\sin\delta}{\cos\delta}\right), \tag{3.23}$$

$$\bar{x} = \frac{x - x_0}{b} \text{ and } \bar{y} = \frac{y - y_0}{a}. \tag{3.24}$$

According to Eq.(3.1), if these parameters are given in at time t, the optical phase $\phi(t)$ is obtained.

3.4.2 Realtime Data Processing

All the PD signals of the GIF are taken by the analog-digital-converter (ADC) and processed in the KAGRA digital system, which is the same as LIGO [58]. The ADC converts the analog signal to the digital signal with 16 bit and 2^{16} Hz) sampling frequency. All the digital signals are simultaneously sampled in the digital system.

The realtime calculation model in the KAGRA system is shown in Figure 3.11. To reduce the calculation cost, the digital signal in this model is downsampled to 2^{14} Hz. This realtime model has three main functions; the ellipse fitting function, the strain calculator function, and the unwrap function. These functions are described below.

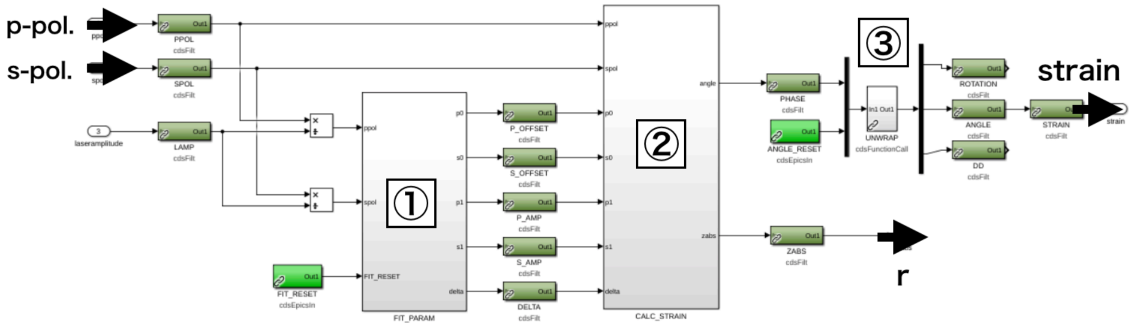

Figure 3.11: Realtime calculation model of the phase calculator of GIF. (1) the elipse fitting function (2) the strain calclator function (3) the unwrap function.

Elipse fitting function

This function is for obtaining the five ellipse parameters in Eq.(**??**) by fitting the ellipse curve to the Lissajous figure drawn by two PD signals. The function calculates these parameters using the least-square method with 512 data points of each two PD signal. These data points are moved every sampling time.

Strain calculator function

This function calculate the optical phase using the ellipse parameters based on Eq.(3.22). For example, Figure 3.12 shows the fitted curve (red line) and the data points (black

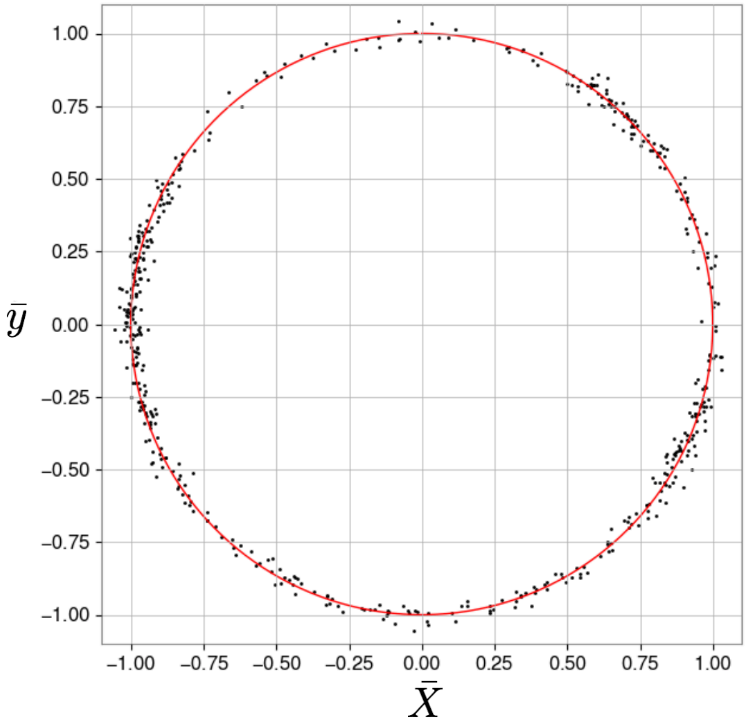

Figure 3.12: Fitting the elipse curve to the Lissajous figure. $\bar{X}$ and $\bar{y}$ are defined in Eq.(3.23,3.24), respectively.

dots). As described above, the optical phase ϕ is an angle of the data point. This optical phase depends on the power ratio $\bar{y}/\bar{x}$ and the phase offset δ because the phase is given by

$$\phi = \frac{\bar{y}}{x}\frac{1}{\cos\delta} - \tan\delta. \tag{3.25}$$

This means that the changes of the power ration and the phase offset are the noise of the optical phase measurement. In particular, the power ratio is sensitive at the PBS, which divides the interfered two polarized lights. For this reason, we covered this location with a small house to protect winds disturbed by passengers. On the other hand, the phase offset has small fluctuation because the QWP is installed in the vacuum chamber.

Although the calculation of the optical phase by measuring the angle is not affected by the input power changes, the signal to noise ratio will worse in less input power. We also monitor the quality of the calculation using a parameter;

$$r = \sqrt{\bar{X}^2 + \bar{y}^2}. \tag{3.26}$$

Unwrap function

This function unwraps the optical phase calculated by the phase calculator function and returns the continuous phase proportional to strain because the atan2 function is used in the phase calculator return between from $-\pi$ to π.

3.4.3 Comparison with seismometers

The two seismometers are installed on the corner area and X-end area, which is separated 3 km. The displacement is calculated by the differential signal of the X direction of these seismometers. On the other hand, because the GIF strainmeter directly measures the displacement of the 1.5 km baseline. Thus, the displacement of the 3 km is calculated by this strainmeter signal multiplied factor 2.

Figure 3.13 shows the ASDs of the displacement of the baseline measured by two seismometers and GIF strainmeter. Above 0.1 Hz, seismometer could measure the displacement, but below this frequency, this is limited by self-noise, which increases in low-frequency. On the other hand, a strainmeter could measure the displacement below 1 Hz. For this reason, we use GIF strainmeter to measure the deformation of the baseline in the low-frequency region, which are the main disturbances degrading the duty cycle of GW detectors.

3.5 Summary of the Chapter

In this chapter, the following items are described:

- Geophysics interferometer (GIF) installed in parallel to the KAGRA X-arm has a strain sensitivity of $\sim 10^{-12}$.
- The advantage of GIF is the wide dynamic range and operation without active alignment control on the mirrors. This feature realizes the long-term stable operation.

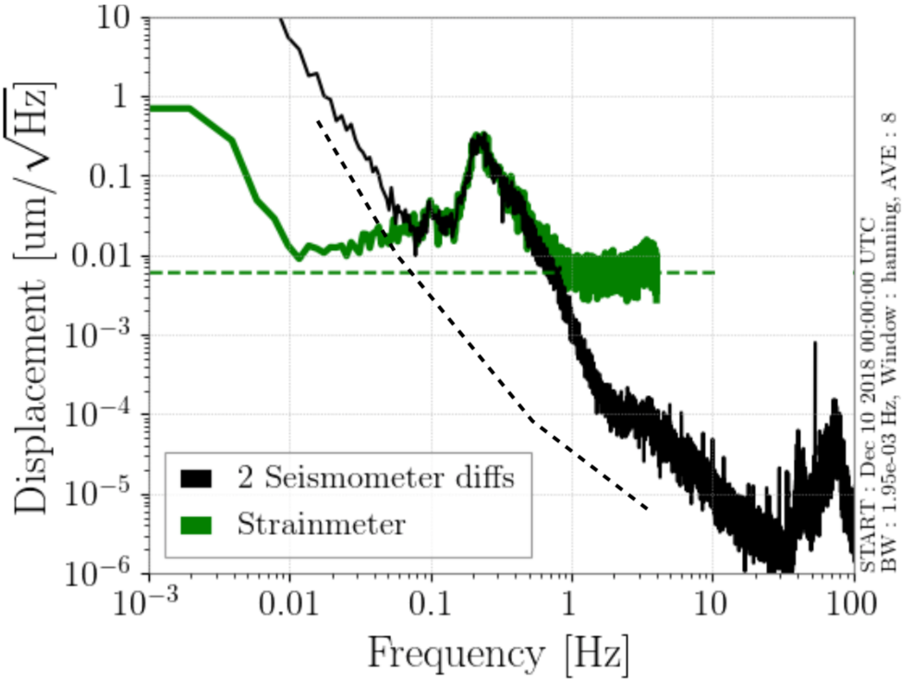

Figure 3.13: Baseline length fluctuation measured by two seismometers (black) and GIF strainmeter (green).

Chapter 4

Baseline Compensation System

The baseline compensation system is one of the active vibration isolation systems for the GW detector's arm cavity.

In the section 4.1, the passive viblation isolation is described. After that, two type of active vibration isolation system are described in the section 4.2 and 4.3. In the section 4.4, the baseline compensation system is described.

4.1 Basics in Seismic Isolation

Essentially, the vibration isolation system has a pendulum to attenuate the seismic noise passively. Actually, the pendulum has developed as a longer and multi-stage pendulum to gain more isolation performance.

4.1.1 Single Pendulum

For a simple example, as shown in the left figure in Figure 4.1, consider a one-dimensional harmonic oscillator consisting of spring with a spring constant k and mass M. The displacement of the suspension point and the mass are x_0 and x, respectively. Because the equation of the motion is written as

$$M\ddot{x} = -k(x - x_0), \tag{4.1}$$

the frequency transfer function from the displacement of the suspension point to the mass displacement $H(f)$ is given by the Fourier transform from the equation and represented as

$$H(f) \equiv \frac{1}{1-(f/f_0)^2}, \tag{4.2}$$

where $f_0 = (k/M)^{1/2}$ is the resonant angular frequency of the oscillator.

According to Eq.(4.2), the amplitude of $H(f)$ is unity below the resonant frequency, the amplitude is approximately proportional to $(f/f_0)^{-2}$ above resonance frequency. The bode plot of $H(f)$ with various resonance frequencies are plotted in right figure in Figure 4.1 . One finds that it is better to make a low-resonance frequency oscillator in order to attenuate the seismic noise broadly.

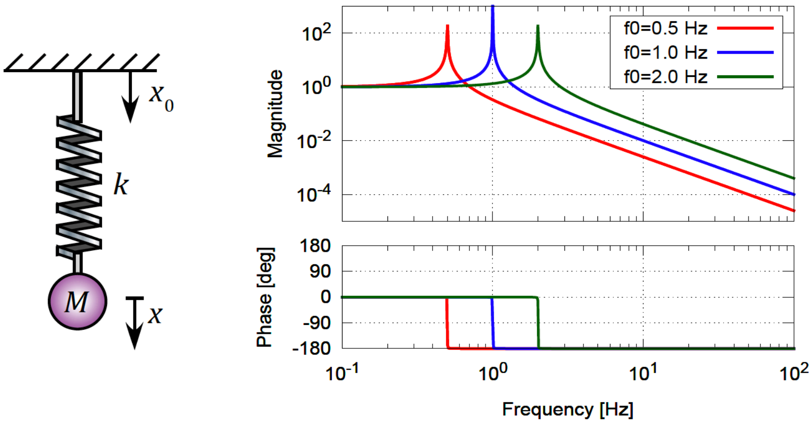

Figure 4.1: Single pendulum as a mechanical filter and its transfer function with various resonant frequencies. This figure is cited from Figure(2.3) in [70].

4.1.2 Multi-stage Pendulum

In order to increase the order of seismic isolation, the multi-stage pendulum is effective. In the case of an N-stage pendulum, the transfer function from the ground to the suspended mass is proportional to f^{-2N} above the resonance frequency of the pendulum, as shown in Figure 4.2.

4.2 Active Inertial Seismic Isolation

The passive vibration isolation cannot reduce the seismic noise below its pendulum's eigenfrequency. To attenuate the lower-frequency seismic noise, the active vibration

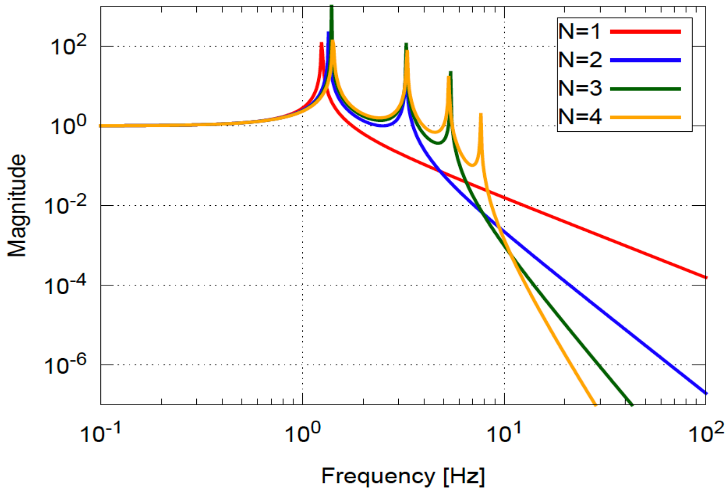

Figure 4.2: The amplitude of the transfer function of the N-stage pendulum. This figure is cited from Figure 2.4 in [70].

isolation system using a seismometer [71].

The active isolation system is shown in Figure 4.3(a). A platform is suspended from the ground with transmissivity H_s. This platform is fed back both signal of an inertial sensor with calibration factor S_H and signal of a relative position sensor with calibration factor S_L, to the platform using actuator with actuator efficiency P_a. This feedback control actively decouples the platform from the seismic disturbance from 0.1 Hz to a few Hz. Moreover, the platform is controlled with feedforward using a seismometer with a calibration factor of S_wit installed on the local ground.

As shown in Figure 4.3(b), the active vibration system is integrated with a feedback control, sensor correction control, and feedforward control. These control schemes are described below.

4.2.1 Sensor Blending Technique

The purpose of the active inertial seismic isolation is to reduce the stage motion against the inertial frame. Thus, we use feedback control using an inertial sensor. However, because the noise level of the inertial sensor is worse in the low-frequency region, the feedback system cannot use the inertial sensor in this region. Nevertheless, to control the DC position of the stage. In this situation, the sensor blending technique is commonly

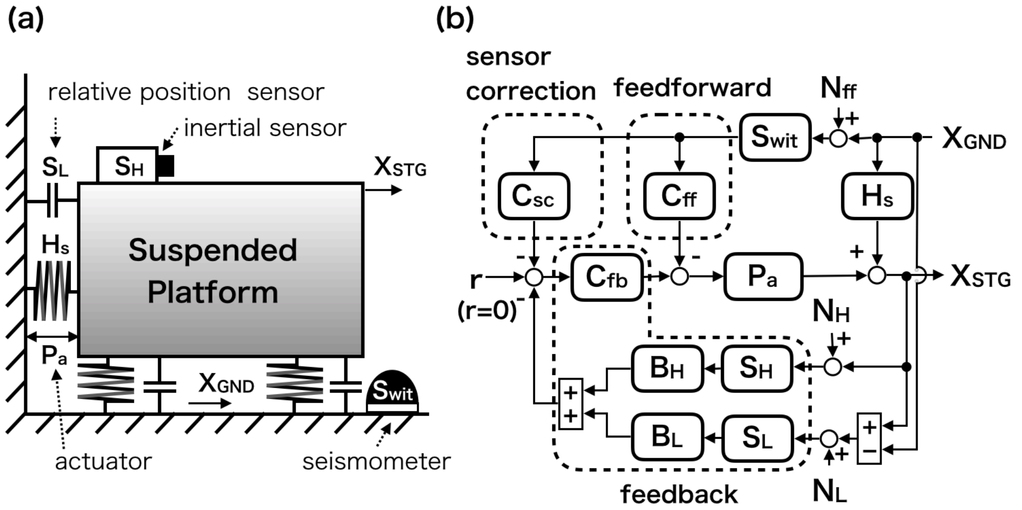

Figure 4.3: **(a)** Schematic drawing of an active seismic isolation system for platform. **(b)** Block diagram of the active control scheme.

used in the active vibration system.

As shown in Figure 4.4, the feedback signal is blended by signals of the inertial and position sensors. The inertial sensor output is filtered with high-pass filter B_{H} because the noise of the sensor is worse in the low-frequency region. On the other hand, the position sensor is filtered with a filter B_{L} so that

$$B_{\mathrm{H}}S_{\mathrm{H}} + B_{\mathrm{L}}S_{\mathrm{L}} = 1, \tag{4.3}$$

In the case of using the blended feedback signal, the displacement of the platform stage. The displacement of the stage is given by

$$X_{\mathrm{STG}} = \frac{G}{1+G}LX_{\mathrm{GND}} + \frac{1}{1+G}H_{\mathrm{s}}X_{\mathrm{GND}} + \frac{G}{1+G}\left(HN_H + LN_L\right), \tag{4.4}$$

where X_{STG}, X_{GND}, N_{H}, and N_{H} are the displacement of the stage and the ground motions, and the noise of the inertial sensor and the position sensor, respectively. Moreover $G = C_{\mathrm{fb}}P_{\mathrm{a}}$ is the loop gain, and the multiples of the comprimentary filters and each sensor responses are defined as $L = B_{\mathrm{H}}S_{\mathrm{H}}$ and $H = B_{\mathrm{L}}S_{\mathrm{L}}$, respectively. Here, if the feedback is work enough, thus the loog gain is large enough, the displacement of the stage is given as

$$\lim_{G\to\infty} X_{\mathrm{STG}} = LX_{\mathrm{GND}} + \left(HN_H + LN_L\right) \tag{4.5}$$

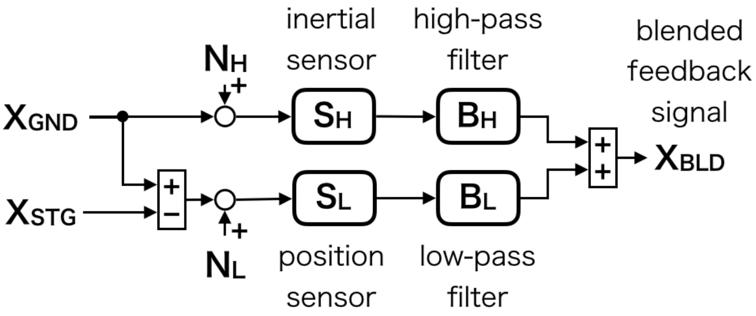

Figure 4.4: Sensor Blending.

According to Eq.(4.5), to isolate the stage against the inertial frame, the active isolation system should design L as small as possible, whereas the H as the complementary filter of that must be large, which means that the inertial sensor noise introduces to the stage. Actually, the cutoff frequency of these filters is chosen at 100 mHz due to the inertial sensor noise, and the system cannot isolate the seismic noise below this frequency. In other words, although the active vibration system using the inertial sensor can design the response from the ground to the stage by filter L, the system performance is limited by the inertial noise in the low-frequency region.

4.2.2 Sensor Correction Technique

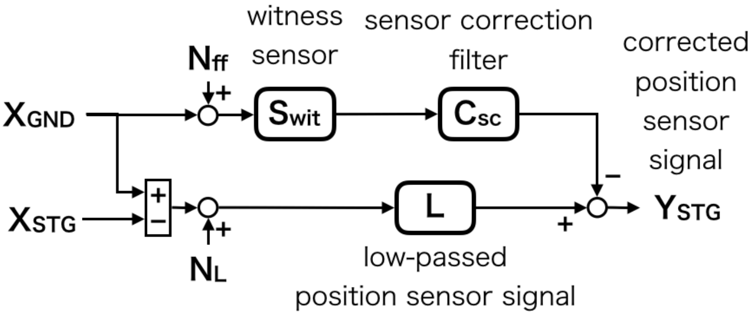

Figure 4.5: Sensor correction scheme.

The sensor correction technique is a method to correct the position sensor using the additional inertial sensor on the ground [72]. As mentioned above, because of the insufficient noise of the inertial sensor on the stage, the blended feedback signal use had to use the position sensor in the low-frequency. This means that the stage motion is reduced against the local ground frame, not the inertial frame in this frequency region. Thus, the sensor correction removes the ground motion from the position sensor by using another seismometer on the ground that has better sensitivity than the inertial sensor on the stage. The corrected feedback signal can compensate for the performance of the inertial sensor on the stage.

Consider the displacement of the vibration isolated stage utilizing the sensor correction technique. As shown in Figure4.3, the correction signal from the seismometer signal is injected at the set-point through the control filter C_{sc} to remove the ground motion from the feedback signal using the position sensor. The displacement of the stage is given by

$$\begin{aligned} X_{\mathrm{STG}} &= \frac{G}{1+G} L \left(1 - C_{\mathrm{sc}} \frac{S_{\mathrm{wit}}}{L}\right) X_{\mathrm{GND}} + \frac{1}{1+G} H_{\mathrm{s}} X_{\mathrm{GND}} \\ &+ \frac{G}{1+G} (H N_H + L N_L) + \frac{G}{1+G} C_{\mathrm{sc}} S_{\mathrm{wit}} N_{\mathrm{ff}} \end{aligned} \tag{4.6}$$

Here, in the case that the loop gain is large enough, the stage motion is given by

$$\lim_{G \to \infty} X_{\mathrm{STG}} = L \Delta_{\mathrm{sc}} X_{\mathrm{GND}} + (H N_H + L N_L) + L N_{\mathrm{ff}}, \tag{4.7}$$

where

$$\Delta_{\mathrm{sc}} \equiv \left(1 - C_{\mathrm{sc}} \frac{S_{\mathrm{wit}}}{L}\right) \tag{4.8}$$

is the gain matching coeffient. By comparison with Eq.(4.7) and Eq.(4.5), the displacement of the stage can be reduced by the gain matching.

Although this gain match factor can be zero when $C_{\mathrm{sc}} = B_{\mathrm{L}}(S_{\mathrm{wit}}/S_{\mathrm{L}})$, actually, the factor is limited by the calibration errors of the witness sensor and the inertial sensor on the stage. At least, the error can not be less than 5%, so it is difficult to achieve the vibration isolation ratio of 20 [72].

4.2.3 Feedforward Technique

The feedforward technique is similar to sensor correction, but this technique removes the motion caused by the ground motion directly. Figure4.6 shows the block diagram of the feedforward control. While the stage motion X_{STG} is disturbed by the ground motion X_{GND} through the mechanical response of the platform H_{s}, the feedforward compensates the stage motion by subtracting the disturbance with the witness sensor

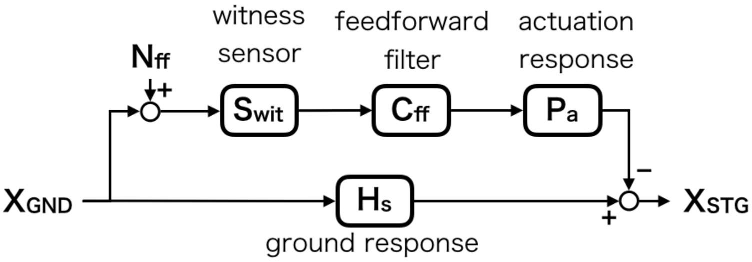

Figure 4.6: Feedforward scheme.

(in this case, seismometer) signal. This feedforward control does not depend on the feedback control, unlike the sensor correction. In other words, the feedforward control works in the frequency region where the feedback loop gain is small, whereas the sensor correction works in the high loop gain region. Therefore, both feedforward and sensor correction technique is used to improve the vibration isolation system in all frequency region.

Finally, consider the control integrated with three techniques; sensor blending, sensor correction, and feedforward. In the case that the additional feedforward signal is injected at the error-point, as shown in Figure 4.3, the displacement of the stage motion is given by

$$\begin{aligned} X_{\mathrm{STG}} &= \frac{G}{1+G} L \Delta_{\mathrm{sc}} X_{\mathrm{GND}} + \frac{1}{1+G} \Delta_{\mathrm{ff}} X_{\mathrm{GND}} \\ &+ \frac{G}{1+G} \left(H N_H + L N_L \right) + \frac{G}{1+G} C_{\mathrm{sc}} S_{\mathrm{wit}} N_{\mathrm{ff}} \\ &+ \frac{1}{1+G} P_{\mathrm{a}} C_{\mathrm{ff}} S_{\mathrm{wit}} N_{\mathrm{ff}}. \end{aligned} \tag{4.9}$$

Here,

$$\Delta_{\mathrm{ff}} \equiv \left(H_{\mathrm{s}} - P_{\mathrm{a}} C_{\mathrm{ff}} S_{\mathrm{wit}} \right) \tag{4.10}$$

is defined as the gain matching coefficient of the feedforward. One can find that, in Eq.(4.9), the first and second terms indicating the contribution from the ground motion can be reduced by the gain matching factors: Δ_{sc} and Δ_{ff}. This reduction works independant from the feedback loop gain.

4.2.4 Problem in Tilt-Horizontal Coupling

The inertial sensors have a problem in horizontal measurement in low-frequency due to coupling from the tilting. This is called the tilt-horizontal coupling. Because of this coupling, the feedback control using the inertial sensor cannot suppress the horizontal seismic motion aggressively.

Tilt-horizontal coupling

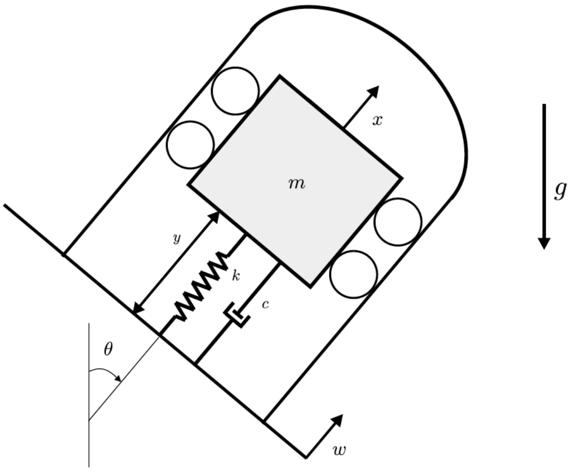

Figure 4.7: Tilted inertial sensor. Cited from Figure12 in [73]

The inertial sensors cannot distinguish the horizontal or tilt motions of the ground because the inertial sensor measure the apparent force from the sensor frame. This coupling is known as the tilt-holizontal coupling and the response from each ground motion is given by [73]

$$Y(s) = \frac{-ms^2}{ms^2 + cs + k} \left[W(s) + \frac{g \sin(\theta_0)}{s^2} \Theta(s) \right], \tag{4.11}$$

where $W(s)$, $Y(s)$, and $\Theta(s)$ are, Laplace transformed, the displacement of the mechanical oscillator in the sensor, the relative displacement of the oscillator and the house enclosuring it, and the tilting angle of the house, respectively. Moreover, m, c, k, g,, and θ_0 are the mass of the osclillator's proof mass, viscous damping coefficient, spring constant, and gravitational acceleration. According to Eq.(4.12), when

$$f < \sqrt{\frac{g\sin(\theta_0)}{(2\pi)^2}}\ [\mathrm{Hz}] \tag{4.12}$$

the tilt motion tends to couple to the horizontal motion. For example, in the case of the maximum tilt coupling: $\theta_0 = \pi/2$, the tilt motion contaminates the horizontal motion when $f < 0.5$ [Hz].

Control strategy to avoid the problem

As described above, the inertial sensor cannot be used for measuring the horizontal motion because of the inertial sensor behaving the tilt sensor. For a reason, the active inertial seismic isolation system in LIGO uses the tilt sensor to remove the tilt components in the inertial sensor for avoiding the tilt-horizontal problem [74].

4.3 Active Baseline Seismic Isolation

For laser interferometric gravitational-wave detector, the baseline length should be isolated from the seismic noise, while it is not necessary to isolate the individual stages to the inertial frame. For this reason, the active baseline seismic isolation system using an additional interferometer named suspension point interferometer (SPI) has been developed.

4.3.1 Suspension Point Interferometer (SPI)

The basic idea of the active baseline vibration isolation is proposed by Drever in 30 years ago. In this idea, the baseline length is kept by feedback or feedforward with the baseline length signal measured by the suspension point interferometer (SPI), which is installed near the suspension point of the pendulum to measure the length [75]. The advantage of this active vibration isolation system is the sensitivity of the SPI, which is better than that of the inertial sensor in low-frequency. Thus, this system could attenuate the seismic noise to DC changes. Therefore, various types of vibration isolation systems have been developed so far.

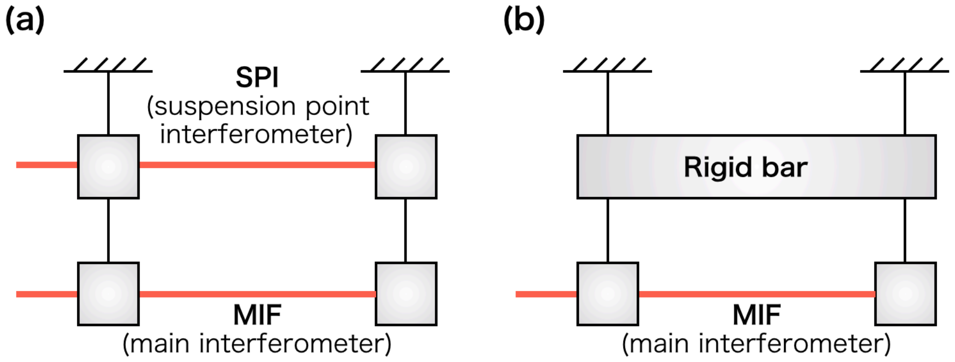

Figure 4.8: Schematic arrangement for one arm of SPI.

Fabry-Perot Optical Cavity Type

The initial type of the SPI is, as shown in Figure 4.8, the Fabry-Perot optical cavity on the main interferometer's arm cavity [76]. The advantage of this idea is that this system can suppress the baseline length fluctuation using the feedback control because the SPI is installed near the main interferometer. Thus, if we increase the feedback gain, the length of the SPI behaves as the rigid bar, as shown in Figure 4.8(b). This means that the main cavity is suspended by the single pendulum from the ground, which does not change the baseline length entirely. Soon, a 2 m prototype of SPI was developed and demonstrated about 40 dB of vibration attenuation below 1 Hz [77].

In general, the disadvantage of SPI is the noise coupling from the common motion due to the worse common-mode rejection (CMR) above the eigenfrequency of the pendulums, because the active baseline vibration isolation system cannot attenuate the common motion of the baseline. If the mechanical response of the pendulums suspended from the SPI stage has asymmetricity, the CMR is worse, and the common motion couples to the baseline length change, which is the differential motion of the baseline.

The Fabry-Perot type SPI has problems in the km-scale GW detectors. While the displacement measurement of the Fabry-Perot cavity is precise, the linear range of the optical cavity is narrow (a few nm). Due to a small dynamic range, the operation of the SPI becomes unstable. As described in section 2.1.2, although the differential motion of a short baseline is reduced efficiently, that of the km-scale baseline is not reduced sufficiently. The reduction of the km-scale baseline is an order of three greater than that of a few meter scale. Moreover, the alignment control is also difficult in the km-scale detectors.

Michelson Interferometer Type

In order to resolve the narrow linear range of the Fabry-Perot type SPI, a prototype of the Michelson type SPI was developed [78]. The interferometer configuration of this prototype was the same as the GIF interferometer, and the signal detection also the same. Thus, the type had a wide dynamic range without alignment control to keep the operation of the SPI. This prototype demonstrates the vibration suppression in 2 m baseline over several hours.

4.3.2 Limitation due to CMRR

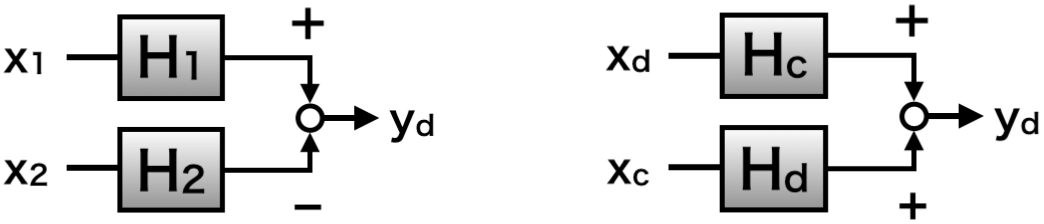

(a) two ground motion inputs (x_1 and x_2) one differential baseline change output (y_d)

(b) two differential and common ground motion inputs (x_d and x_c) one differential baseline change output (y_d)

Figure 4.9: comparison of two representations.

While the active inertial seismic isolation described in section **??**, the active baseline seismic isolation cannot isolate the common motion. Thus, if worse common-mode rejection (CMR) of the suspensions, the common ground motion couples to the differential ground motion, which is the baseline length changes.

Consider the differential motion of the platform stages. As shown in Figure 4.9a, the motion can be represented as

$$y_\mathrm{d} = H_1 x_1 - H_2 x_2, \tag{4.13}$$

where x_i, y_d and H_i denote the ground motion, the stage motion, and the mechhanical transferfunction from the ground motion to the stage motion, respectively. The indicies of i run in 1 or 2, which denote the name of the stages. Here, we define the differential and common motion of the ground and transferfunction as

$$x_{\rm d} = x_1 - x_2,\ \ x_{\rm c} = x_1 + x_2 \tag{4.14}$$

$$H_{\rm d} = \frac{H_1 - H_2}{2},\ \ H_{\rm c} = \frac{H_1 + H_2}{2}. \tag{4.15}$$

The Eq(4.13) can be represented as

$$y_{\rm d} = H_1 x_1 - H_2 x_2 \tag{4.16}$$

$$= H_{\rm c} x_{\rm d} + H_{\rm d} x_{\rm c}. \tag{4.17}$$

The last equation can be represented as shown in Figure 4.9b. Moreover, if we define the CDMRR of this system as

$$H_{\rm CMRR} \equiv \frac{H_1 + H_2}{H_1 - H_2} = \frac{H_{\rm c}}{H_{\rm d}}, \tag{4.18}$$

the differential system can be written as

$$y_{\rm d} = H_{\rm c}\left(x_{\rm d} + \frac{1}{H_{\rm CMRR}} x_{\rm c}\right) \tag{4.19}$$

Eq.(4.19) indicates that increaseing the CMRR, the coupling from the common ground motion to the differential stage motion. In other words, the inverse of the CMRR is the coupling coefficient.

According to the definition of The CMRR, this factor is sensitive to the differential of two mechanical response. Thus, if the eigenfrequency of each pendulum, the CMRR is worse above the frequency. For example, assume that the mechanical response of the stage is the single pendulum, which transfer function from the ground to the stage can be given by Eq.(4.2). In the high frequency, above the eigenfrequency, the response can be approximate as $H \sim (f_0/f)^2$. In this frequency region, if the eigenfrequency shifts by Δf_0, the gain of the response differs by $2f_0\Delta f_0$. This amount worse the CMRR, and the common motion contaminates the differential motion.

4.3.3 RMS Reduction

The reduction of Root-mean-square (RMS) of the differential stage motion is expected by utilizing the SPI on the active seismic isolation system. Because the SPI has good sensitivity in low-frequency, including the microseisms and earth tides, the RMS of the differential stage motion can be reduced.

The reduction has some advantages for GW detectors.

Improvement of Actuator Noise

The RMS reduction of the differential stage motion can relax the requirement of the actuator on the test mass. The actuator on the test mass can only actuate weak force because the strong actuator would introduce the actuation noise to the sensitivity [79]. Therefore, the RMS reduction on the top stage can reduce the load on the test mass actuators. This means the improvement of the test mass actuator's noise directly, moreover, means that the actuator's dynamic range can become wider.

Improvement of Glitch Noise

The reduction of the test mass actuator's load reduces the glitch noise, such as the Barkhausen noise. This noise is caused by the large DC voltage on the test mass actuators and actuators above the test mass [80].

4.4 Baseline Compensation System

The baseline compensation system is the active baseline seismic isolation system using the GIF.

4.4.1 Purpose

The purpose of the baseline compensation system is to reduce the RMS of the cavity length fluctuation from 1 Hz to DC. In this region, the RMS motion in cavity length is mainly disturbed by the seismic noise such as the microseisms ($\sim 200\,\mathrm{mHz}$), large earthquake in distant place ($< 100\,\mathrm{mHz}$), air pressure response ($< 20\,\mathrm{mHz}$), and earth tides ($\sim 10^{-5}\,\mathrm{Hz}$). Moreover, the RMS of these seismic motion is comparable with several $1 \sim 100\,\mathrm{um}$, which is much greater than the test mass actuator's range. Therefore, the compensation of the cavity length disturbed by these seismic noises not only the improve stability of the detector operation but also reduces the glitch noises in the GW signal.

4.4.2 Concept

The concept of the baseline compensation system is the feedforward control, which moves the platform stage at X-end using the baseline length changes measured by the GIF in order to compensate for the seismic disturbance, as shown in Figure 4.10. The cavity's mirrors are suspended by the pendulums, whose suspension point is fixed on the platform stage. This platform stage is also suspended by the inverted pendulums on the second floor. The platform responds to the seismic motion below 1 Hz, which is the target frequency to be reduced. Thus the seismic disturbance of the stage motion is attenuated by using the actuator on the stage. The control signal is given by the GIF on the first floor.

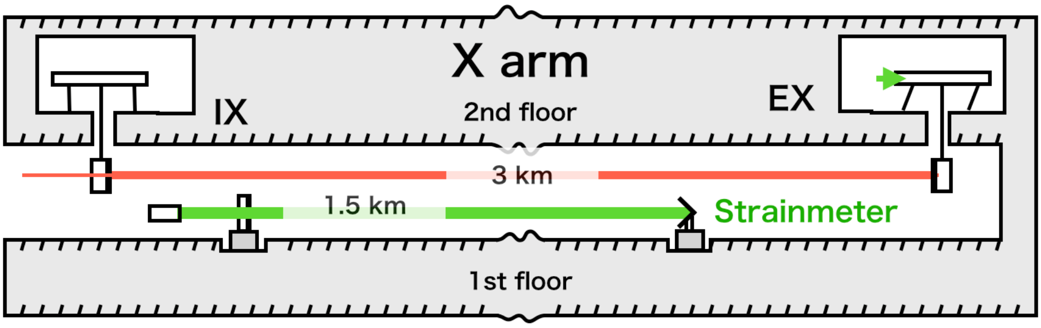

Figure 4.10

4.4.3 GIF as a SPI

The idea of this baseline compensation system originates from the [78] as mentioned in section 4.3.1. While this system used feedback control, our system uses feedforward control. The feedback control style baseline compensation system has some difficulty in terms of developing the km-scale system because we need to install the SPI, which measure the baseline length should be installed on the platform stage. This means that, in KAGRA case, an additional tunnel is needed on the second floor to connect the platform stages. On the other hand, the feedforward style system does not need such a facility; it just requires the SPI, which can measure the baseline length in the target frequency, which is below 1 Hz.

In terms of the low-frequency, the difference between the length change of 1500 m baseline and that of 3000 m baseline is differed by factor 2, according to Figure 3.5.

4.4.4 Control methods

We describe the general control scheme of the active baseline seismic isolation system using the feedforward type SPI. In this case, because of no feedback type SPI, the

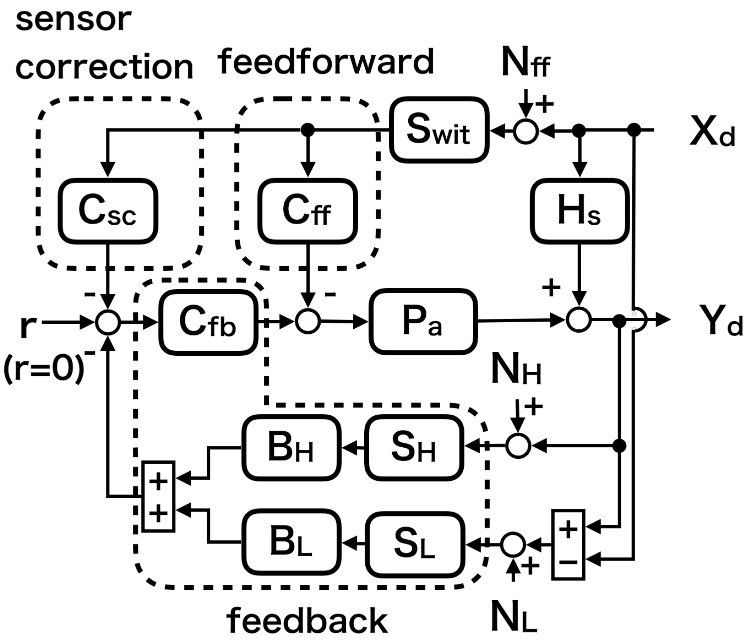

Figure 4.11: The block diagram of the active baseline seismic isolation system.

baseline length is controlled by using the inertial sensor and relative position sensor as well as the active inertial isolation system. However, the additional control schemes, such as the sensor correction and the feedforward, are implemented in this new system.

The baseline isolation system attenuates, of course, the cavity length fluctuation. This fluctuation is the differential component of the displacement of each test mass. To simplify the discussion, we supposed the CMRR is large enough to ignore the common motion coupling. Thus, we can just consider the only differential component of the motion in this system.

The control diagram of the active baseline isolation system can be represented as shown in Figure 4.3. Essentially, all the terms in this figure are the same as the active inertial isolation system shown in Figure 4.3 except the input and output signals. Their signals are replaced as X_d and Y_d, which are the differential displacement of the ground and platform stage motions, respectively. In this figure, S_wit and N_ff are the frequency response and the self-noise of the GIF, respectively. Furthermore, the noises N_H and N_L are multiplied by $\sqrt{2}$ in the case of the amplitude unit.

The displacement of the differential motion of the stages is given by

$$\begin{aligned} Y_{\mathrm{d}} &= \frac{G}{1+G} L \Delta_{\mathrm{sc}} X_{\mathrm{d}} + \frac{1}{1+G} \Delta_{\mathrm{ff}} X_{\mathrm{d}} \\ &+ \frac{G}{1+G} \left(H N_H + L N_L \right) + \frac{G}{1+G} C_{\mathrm{sc}} S_{\mathrm{wit}} N_{\mathrm{ff}} \\ &+ \frac{1}{1+G} P_{\mathrm{a}} C_{\mathrm{ff}} S_{\mathrm{wit}} N_{\mathrm{ff}}. \end{aligned} \tag{4.20}$$

As described about the active inertial seismic isolation system in section **??**, both the additional reduction factors Δ_{sc} and Δ_{sc} can isolate the differential ground motion X_{d}. Although the witness sensor was the inertial sensor in the previous iolation system, the new isolation system use the GIF, which can measure the seismic noise below 1 Hz and to DC. This is the advantage.

4.5 Summary of the Chapter

In this chapter, the following items are described:

- While the passive isolation system could isolate the seismic noise above its eigenfrequency, which is typically around 1 Hz, the active isolation systems are needed to compensate for the low-frequency seismic noise below 1 Hz by isolating the platform stage from the seismic noise.

- Two active isolation systems are described; the active *inertial* seismic isolation system attenuates the platform stages to the inertial frame, the active *baseline* seismic isolation system isolates the optical arm cavity's length from the deformation of the baseline.

- The performance of the active inertial seismic isolation system is limited by the insufficient sensitivity and the tilt-horizontal coupling of the inertial sensor below 100 mHz.

- Although the active baseline seismic isolation is an effective method, the SPI, which is the cavity length monitor, has difficulties in the longer scale GW detector.

- The baseline compensation system using the GIF strainmeter resolves these limitations and problems because the strainmeter can measure the deformation of the baseline below 1 Hz without tilt-coupling, and the strainmeter can observe the baseline fluctuation independent from independent of the GW detector.

Chapter 5

Demonstration of Baseline Compensation System

In this chapter, the demonstration of the baseline compensation system is described. The purpose of this demonstration is to compensate for the deformation of the baseline so that the length fluctuation of the 3-km arm cavity is reduced below 1 Hz, where the passive seismic isolation cannot attenuate the seismic disturbance.

In the section 5.1, experimental arrangement for demonstration is described. In section 5.2, the result of the test is described. In the end, the discussion is described in section 5.3.

5.1 Experimental Arrangement

Because the purpose of the baseline compensation system is to reduce the arm cavity length fluctuation, we prepared the experimental arrangement to measure the length.

5.1.1 Measurement of X-arm cavity length

The length fluctuation of the X-arm cavity is measured by the PDH method [81]. This method obtains the error signal, which is proportional to the displacement from the nominal length where the cavity is on resonance. In order to keep the resonance, the error signal is fed back to the acousto-optics modulator (AOM), which changes the input laser frequency.

Brief measurement procedure is shown in Figure 5.1. (1) The deformation of the baseline causes the length change of the arm cavity length through the suspensions. Suppose that the baseline length is displaced by ΔL from the nominal length of L. Utilizing the PDH method, we can obtain the error signal proportional to this displacement. (2) This signal is also interpreted as the frequency changes of the input laser because the frequency change Δf has a relation with the baseline length change ΔL [35];

$$-\frac{\Delta f}{f} = \frac{\Delta L}{L}. \tag{5.1}$$

(3) To keep the optical cavity on resonance, the signal is fed back to the AOM, which is the frequency actuator. In this procedure, the length fluctuation is obtained from the feedback signal to the AOM.

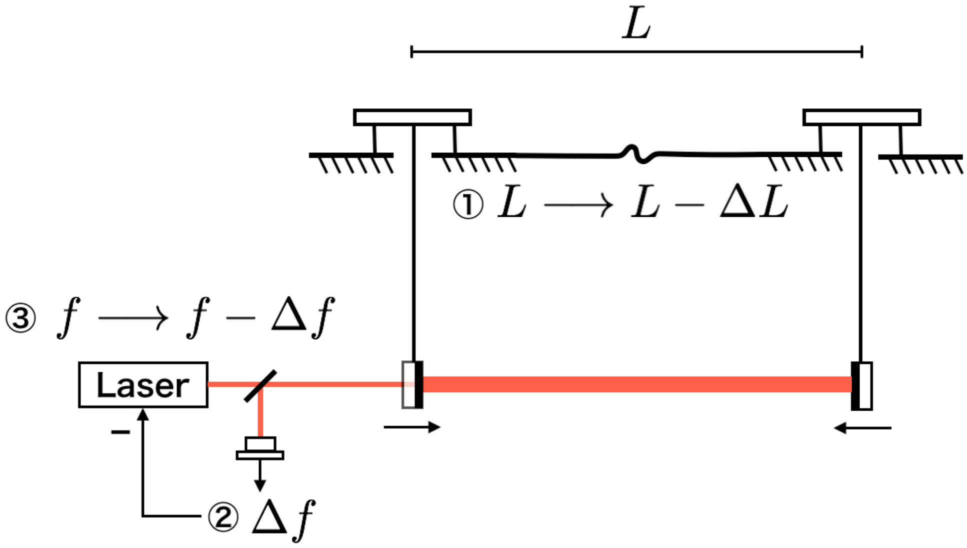

Figure 5.1: Experimental arrangement for X-arm length measurement. X-arm cavity controled by feeding the PDH signal back to the AOM of the input laser to keep on resonance. The length change of the cavity is obtained from the feedback signal.

5.1.2 Control Design

To demonstrate the baseline compensation system using GIF, we design a simple control configuration. Although the simplest configuration is the feedforward using the GIF, the feedforward control cannot suppress the disturbances other than the horizontal seismic noise such as the tilt ground motion or the temperature fluctuation [70]. Because these disturbances could move the platform stage in a horizontal direction, we need a feedback

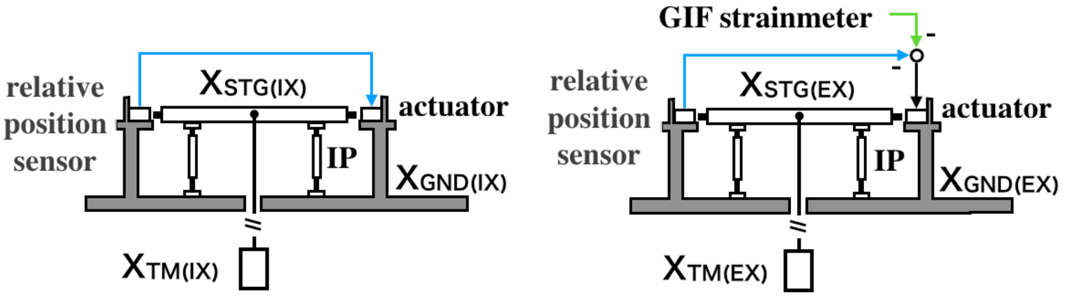

(a) Schematic contol of each platform stage. Left figure is that of the IX stage, right figure is that of the EX.

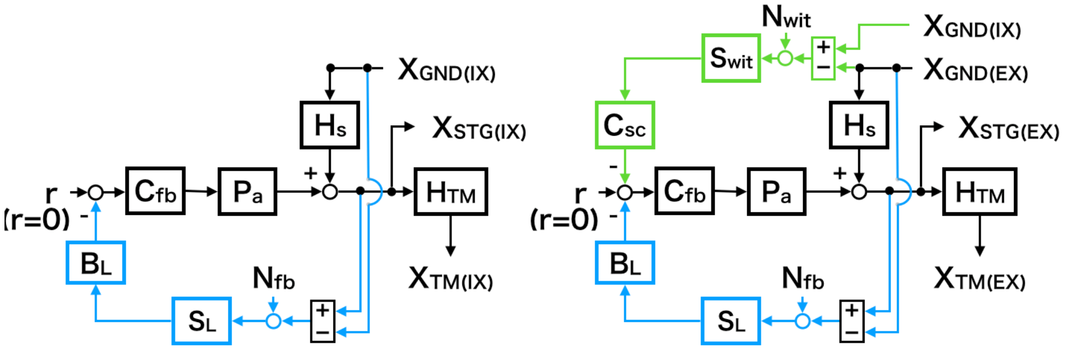

(b) Control block diagram of each platform stage. Left figure is that of the IX stage, right figure is that of the EX.

Figure 5.2: The baseline compensation control of each platform stage for demonstration.

control using the position sensor to suppress these disturbances. Therefore we use the sensor correction control rather than the feedforward control.

Figure 5.2a shows the schematic control of the platform stage for the input x-arm test mass (IX) and end x-arm test mass (EX). While the IX stage is fed back the relative position sensor signal to the actuator on the stage, the EX stage is added to the GIF strainmeter signal. In other words, while the IX stage is locked to the local IX ground, the EX stage is also locked to the local EX ground, but this feedback signal is corrected by using the GIF strainmeter. The GIF measure the baseline length changes, which means the differential motion of the IX and EX ground. Therefore, the feedback signal corrected by using GIF is the same as the feedback signal of the IX stage. Thus, the EX stage can follow the IX stage by using the corrected feedback signal.

Figure 5.2b shows the control diagram of each stage. In both stages, the displacement of the IX platform stage X_{STG} is disturbed by the local seismic motion X_{GND} though the mechanical response of the inverted pendulum (IP) H_{s}. Moreover, the displacement of the IX test mass is also disturbed by this seismic noise through the mechanical response of the pendulum H_{TM}. In order to reduce the test mass motion in the low-frequency region, below 1 Hz, the platform stage is controlled by the feedback control using the relative position sensor. S_{L}, N_{fb} and B_{L} are the displacement response and the noise of the relative position sensor and the low-pass filter not to inject the sensor noise to the feedback signal. The feedback signal is sent to the actuator, whose transfer function from the actuator force to the platform stage is given by P_{a}, through the control filter C_{fb}. On the other hand, the feedback signal of the EX stage is corrected by the GIF signal.

In this situation, each displacement of the stage are given by

$$\begin{aligned} X_{\mathrm{STG(IX)}} &= \frac{G}{1+G}X_{\mathrm{GND(IX)}} + \frac{G}{1+G}N_L + \frac{1}{1+G}H_{\mathrm{s}}X_{\mathrm{GND(IX)}} \quad (5.2) \\ , X_{\mathrm{STG(EX)}} &= \frac{G}{1+G}\left(1-\frac{C_{\mathrm{sc}}S_{\mathrm{wit}}}{B_{\mathrm{L}}S_{\mathrm{L}}}\right)X_{\mathrm{GND(EX)}} + \frac{G}{1+G}N_L \\ &+ \frac{G}{1+G}\frac{C_{\mathrm{sc}}S_{\mathrm{wit}}}{B_{\mathrm{L}}S_{\mathrm{L}}}X_{\mathrm{GND(IX)}} + \frac{G}{1+G}\frac{C_{\mathrm{sc}}S_{\mathrm{wit}}}{B_{\mathrm{L}}S_{\mathrm{L}}}N_{\mathrm{wit}} \\ &+ \frac{1}{1+G}H_{\mathrm{s}}X_{\mathrm{GND(EX)}}, \quad (5.3) \end{aligned}$$

respectively, where $G = C_{\mathrm{fb}}P_{\mathrm{a}}S_{\mathrm{L}}B_{\mathrm{L}}$ is the loop gain. Here, if $G \gg 1$ and we design the sensor correction filter C_{sc} so that

$$\frac{C_{\mathrm{sc}}S_{\mathrm{wit}}}{B_{\mathrm{L}}S_{\mathrm{L}}} = 1, \quad (5.4)$$

the displacement of each stage are give as

$$\begin{aligned} X_{\mathrm{STG(IX)}} &= X_{\mathrm{GND(IX)}} + N_{\mathrm{L}}, \quad (5.5) \\ X_{\mathrm{STG(EX)}} &= X_{\mathrm{GND(IX)}} + N_{\mathrm{L}} + N_{\mathrm{wit}}. \quad (5.6) \end{aligned}$$

Moreover, if the noise of the GIF, which is the wittness sensor is smaller than that of the relative position sensor, both stage motions are the same each other; $X_{\mathrm{STG(EX)}} = X_{\mathrm{STG(IX)}}$. This same motion means the reduction of the differential stage motion. Thus, the cavity length is isolated from the differential ground motion, which is the baseline length fluctuation.

5.2 Results and Discussion

The performance of the baseline compensation system is evaluated when the system is engaged.

5.2.1 Results

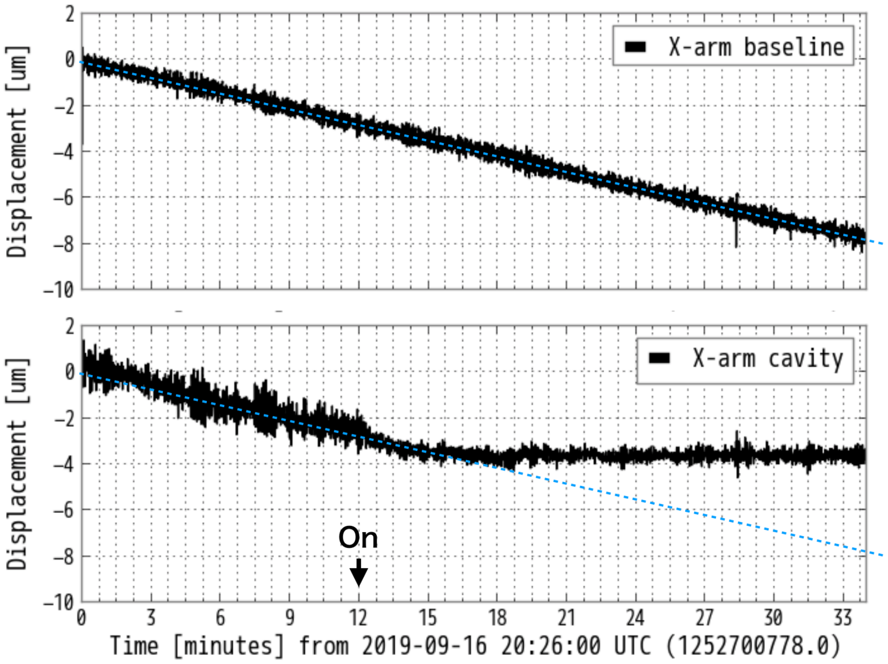

Figure 5.3: Length change of both X-arm baseline and X-arm cavity when baseline compensation system is turned on or off. At 12 minutes, the control is on.

Figure 5.3 shows the length fluctuation of the arm cavity and of the baseline as a reference. At 12 minutes, the baseline compensation system was turned on. Whereas the X-arm cavity length is drifted during the compensation system was off, the drift is removed during the system was on. This drift is comparable to the earth tide. As a result, this system compensated the deformation of the baseline, and the reduction ratio is almost 1/10.

This result also indicates that the RMS amplitude of the X-arm cavity length is reduced. The amplitude spectrum density of the length when both the compensation system was on and off is shown in Figure 5.4. It is clear that the accumulated RMS amplitude is reduced due to the compensation system. In the next, we compare this measured data with the rigid body model.

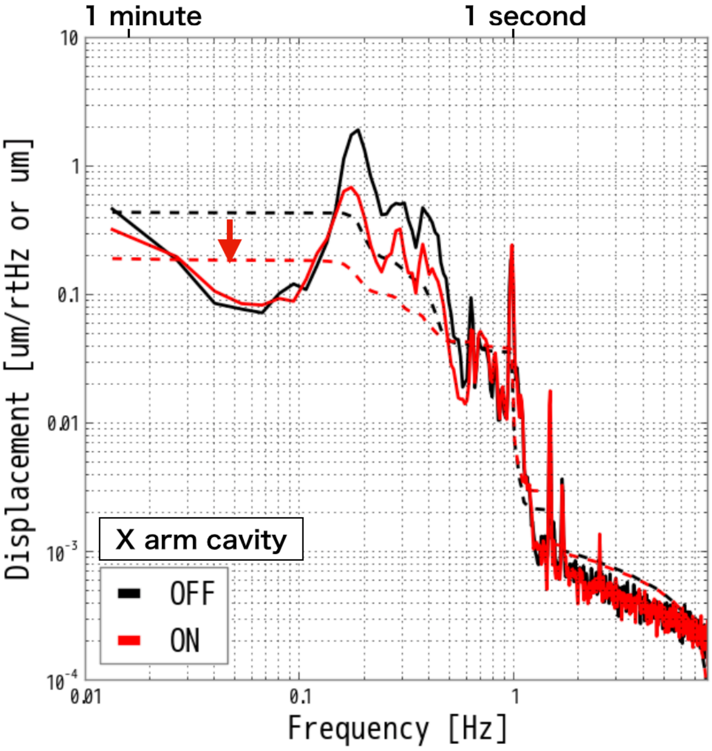

Figure 5.4: ASDs of X-arm caivty length when baseline compensation system is turned on and off.

Comparison with the model

Compare with the measured data and rigid body model of the KAGRA suspensions [70]. Because this model outputs the state-space model, we can calculate the transfer function. For example, the transfer function from the ground motion to each stage; the platform stage, test mass, and so on.

To simplify the discussion, suppose the CMRR is large enough to ignore the coupling from the common motion to the differential motion, as described in 4.3.2. It is a valid assumption below the eigenfrequency of the suspensions. According to Eq.(4.19), the transfer function from the differential input to differential output is given by a single transfer function. Therefore, the differential transfer functions from the differential ground motion to the differential output of the stage and the test mass motion are given by the single transfer function of that, respectively.

Figure 5.5a shows the amplitude spectrum densities (ASDs) of the X-arm cavity length when the compensation system is OFF. The black line is the ASD calculated by the feedback signal of the X-arm cavity. The red line is the ASD, which is the summation of the noise contributions, the noise of the relative position sensor, named LVDT (blue line), and the noise of the differential baseline length change measured by the GIF strainmeter (orange line). Above 1 Hz, the X-arm cavity length and the seismic noise contribution are not the signals due to the noises of the instruments. Below 1 Hz, the measurement is consistent with the estimation.

Figure 5.5b shows the ASDs of the X-arm cavity length when the compensation system is ON. The red line, which indicates the summation of the noise contribution estimated by the rigid body model, is calculated assuming the reduction factor of the sensor correction of 1/20, as mentioned in 4.2.2. This reduction factor is calculated from the relative calibration error of 5 % between the LVDT and GIF. Although this reduction rate should be realized, the measurement is not consistent with the estimation assumed the reduction rate. The RMS of the cavity length fluctuation is limited by peaks around 200 mHz.

5.2.2 Discussion

The peaks around 200 mHz, which are the main contributions to the RMS, are correlated with the other degrees of freedoms (DOFs).

Figure 5.6 shows the ASDs in the top figure and the coherence in the bottom figure when the compensation system was off. In the top figure, the ASDs of the X-arm cavity length and the baseline length changes are displayed. The baseline length changes are shown by two ASDs; the length change measured by the GIF strainmeter and that given by the differential signal of two seismometers, which is installed near the IX and EX stages. While, above 1 Hz, the baseline length change should be referred by the seismometer differential signal, below 50 mHz, the length change should be referred by the GIF strainmeter signal because of this self-noise. One can find that the X-arm cavity length is enhanced by some mechanical peaks compared with the baseline length change. On the other hand, the bottom figure shows some coherence between the X-arm cavity length and the GIF, and between the cavity length and the other DOFs' signals; the feedback signals of the yaw and transverse directions on the each IX and EX platform

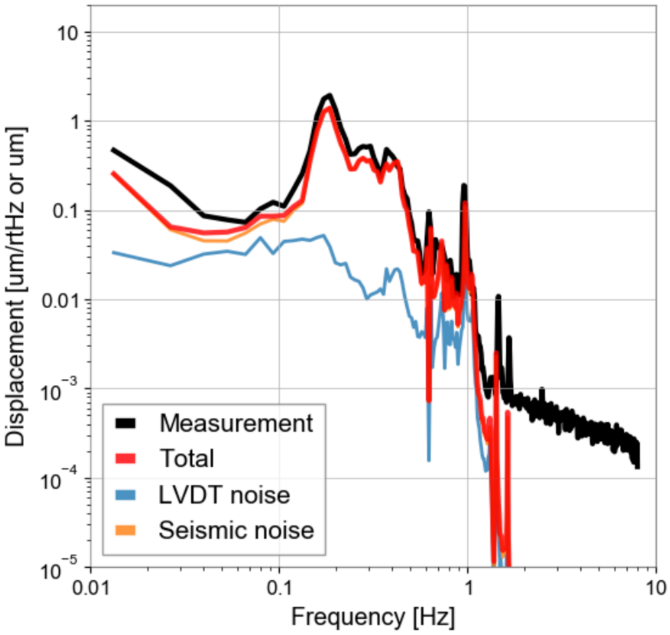

(a) Noise budget when the compensation system is OFF. Measurement is same as the black line in Fig.5.4. Total is the summation of all the noise contributions.

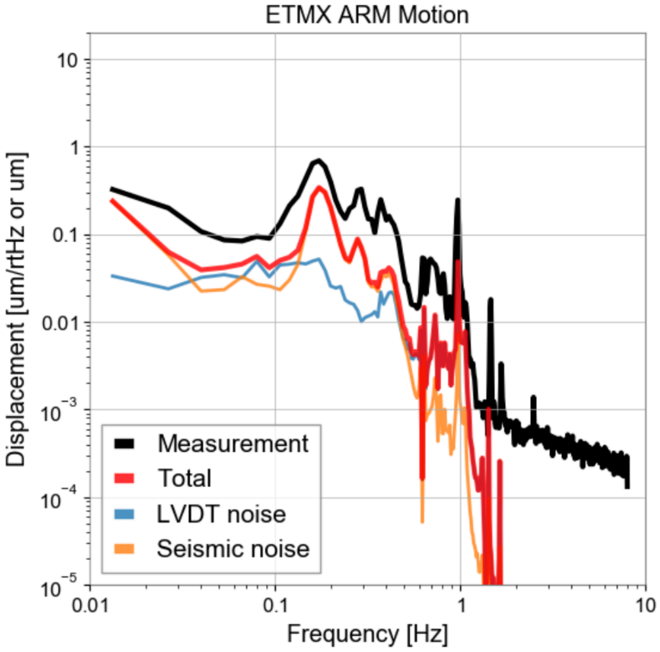

(b) Noise budget when the compensation system is ON. Measurement is same as the red line in Fig.5.4. Total is the summation of all noise contributions assuming the reduction factor of sensor correction of 1/20.

Figure 5.5: Comparison between the measurement of X-arm and expected value of that. The expected total value is the summation of some noise contribution, which is named noise budget.

stages, which controls are needed to keep the X-arm cavity on resonance. Whereas the cavity length has a coherence with the deformation of the baseline measured by GIF strainmeter (blue) around 0.2 - 0.7 Hz broadly, coherence with the other DOFs does not exist clearly in this frequency region. This coherence implies that the cavity length is mainly disturbed by the deformation of the baseline.

Figure 5.7 show the ASDs and coherence when the compensation system was on. Around 0.2 Hz, the coherence between the cavity length and the many other DOFs appear, although these coherences did not when no length compensation. These coherences imply the cavity length is disturbed by the internal DOFs coupling.

5.3 Summary of the Chapter

In this chapter, the following items are described:

- Experimental arrangement for evaluation of the X-cavity length fluctuation was described.
- As a result, above 1 minutes period, the fluctuation is reduced by 20 dB, while below this period, the fluctuation is reduced by 6 dB.
- According to the coherence measurement, the internal coupling to the cavity length would limit the performance in the short period region.

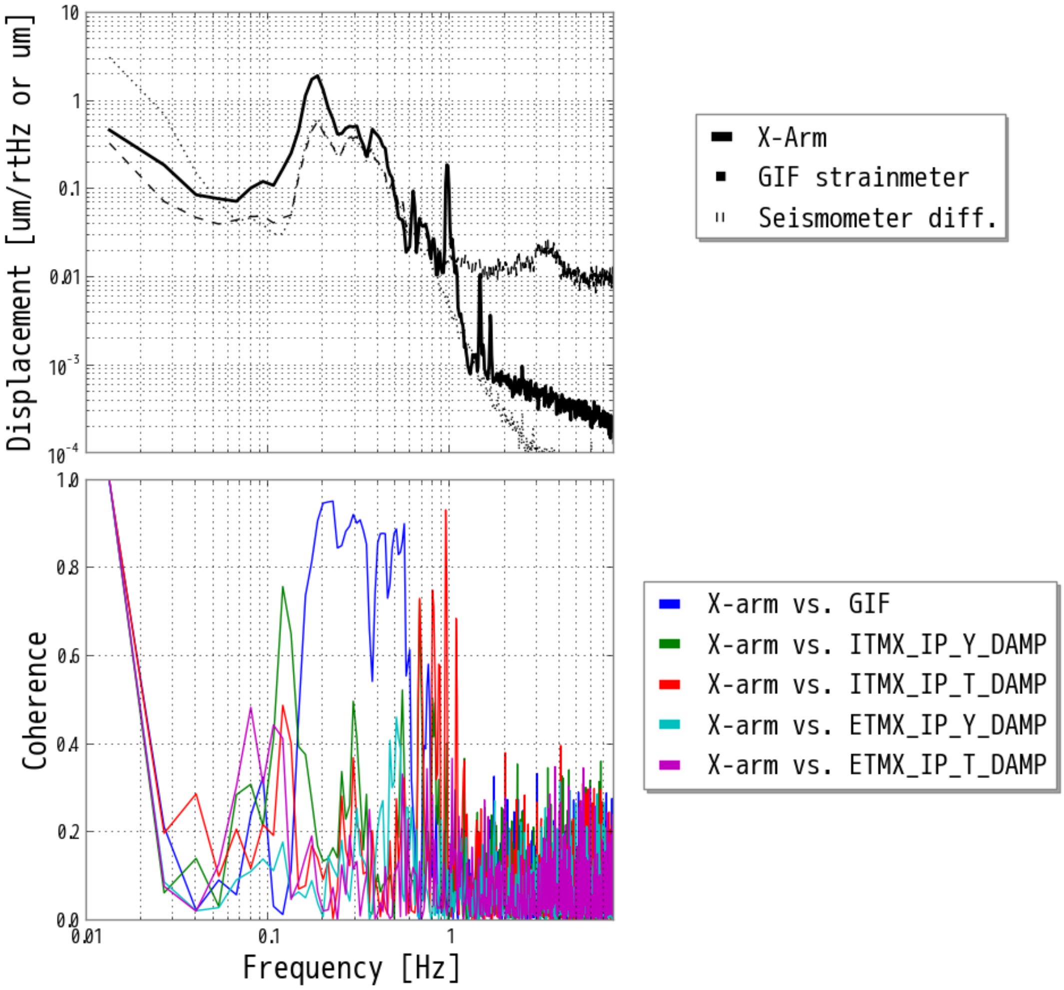

Figure 5.6: Coherence between the cavity length and GIF strainmeter, other degrees of freedoms on the stage control when the compensation system is on. (Top) ASD of the cavity length and baseline length. (Bottom) The coherence between the cavity's length and some signals.

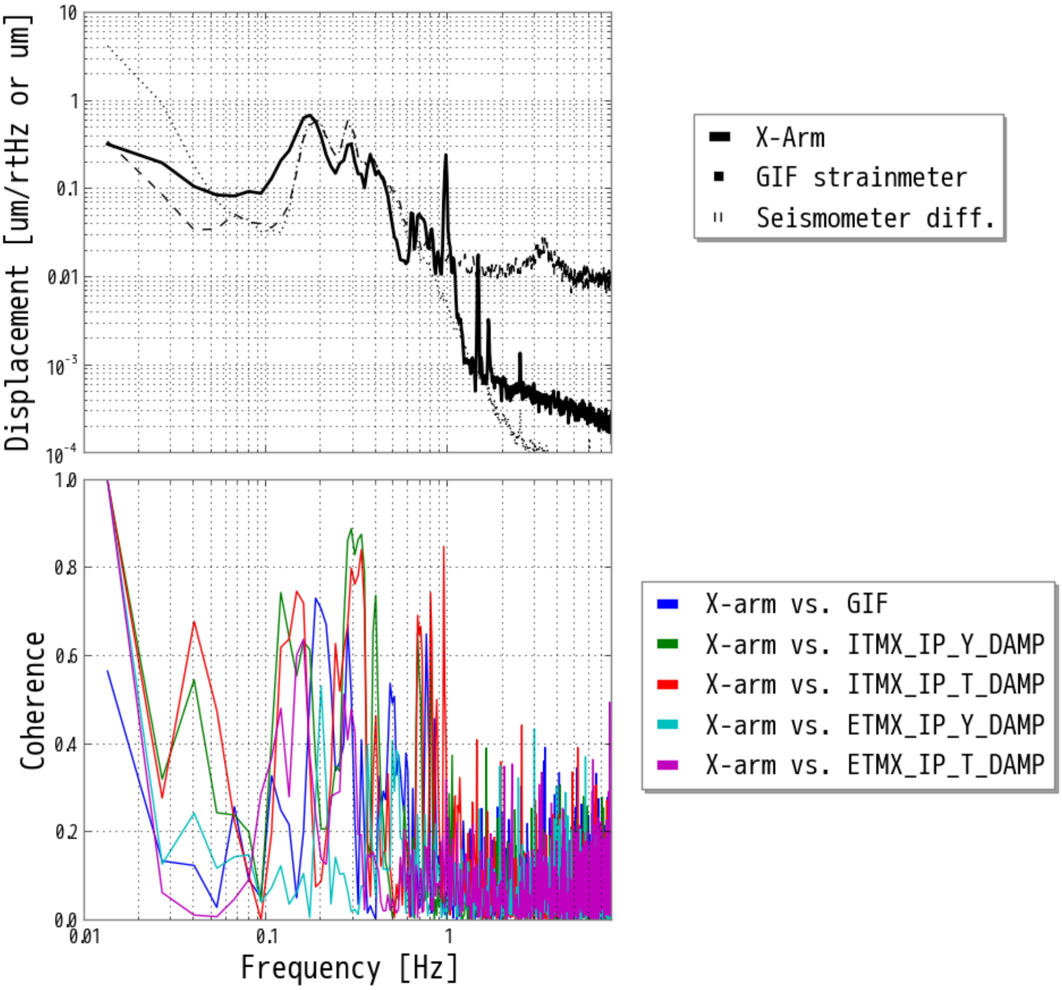

Figure 5.7: Coherence between the cavity length and GIF strainmeter, other degrees of freedoms on the stage control when the compensation system is off. (Top) ASD of the cavity length and baseline length. (Bottom) The coherence between the cavity's length and some signals.

Chapter 6

Conculusion and Future Directions

6.1 Conclusion

The conclusion is below:

- The low-frequency seismic noise is a problem for the stable operation of the km-scale baseline GW detectors.
- The baseline compensation system is developed and demonstrates the reduction of the cavity length fluctuation below 1 Hz.
- This baseline compensation system is an important role to improve the duty cycle of the current and future GW detectors

6.2 Future Directions

In order to improve the isolation performance from 0.1 to 1 Hz where our compensation system could not reduce effectively, of course, the internal DOFs coupling should be resolved firstly, but the active inertial seismic isolation is needed. Through the study of the baseline compensation system, we obtained some prospects for improving the seismic isolation system. The prospects are below:

- Above 1 Hz, the observation frequency band for the GW detector, the passive vibration isolation system using the multi-stage pendulum, should be used.
- From 0.1 Hz to 1 Hz, the eigenfrequencies of the pendulums, the active inertial seismic isolation system using the inertial sensor should be used, because this

system can suppress both common and differential motion of the arm cavity. This advantage can resolve the problem that the active baseline isolation system has due to the CMRR of the cavity's mechanical response.

- Below 0.1, the frequency where the sensitivity of the inertial sensor is worse, the active baseline seismic isolation system using the GIF strainmeter should be used.

This seismic isolation system optimized in these three frequency regions will improve the operation stability of current and future GW detectors.

Appendix A

KAGRA

A.1 Overview of KAGRA

A.1.1 Status of KAGRA

KAGRA is a 3km laser interferometer constructed in Kamioka, Gifu, Japan, and is now in its final commisioning phase. KAGRA is now commisioning to observe with LIGO and Virgo in the third observation (O3), through the two test operation phase. The phases of KAGRA project is listed in Table **??**. The first test operation named initial KAGRA (iKAGRA), which is taken place from March to April 2016, was a demonstration of the 3-km Michelson interferometer. In this operation, While the test masses are not in cyogenic temperature but room temperature, KAGRA demonstrate the operation of the km-scale interferometer in the underground. Next, the second test operation named baseline KAGRA (bKAGRA) demonstrated the cryogenic Michelson interferometer from April to May 2018. Although this interferometer was not for sensitivity enhanced configuretion, the cryogenic operation, which is the key feature of KAGRA, could be demonstrated. Now, December 2019, KAGRA is faced on the O3 observation with the Michelson interferometer whose each arm have Fabry-Perot optical cavities (FPMI). To join the O3, KAGRA is now tunning the interferometer operation and hunting the sevelal technical noises.

A.1.2 Main Interferometer

The main interferometer of KAGRA is shown in Figure A.1a. The interferometer configuration of KAGRA is also the same as other GW detectors such as advanced LIGO

Table A.1: Summary of the phasec of KAGRA. MI: Michelson Interferometer, FPMI: Fabry-Perot Michelson Interferometer, DRFPMI: Dual-Recycled Fabry-Perot Michelson Interferometer, RSE: resonant sideband extraction

	iKAGRA	bKAGRA Phase1	bKAGRA for O3	bKAGRA (final)
Year	2016 Mar - Apr	2018 Apr - May	2019 Dec -	2020 - (planned)
Configuration	MI	MI	FPMI	DRFPMI (RSE)
Test mass temperature	room temp.	18K room temp.	18K room temp.	22K

and advanced Virgo, the Michelson interferometer with Fabry-Perot optical cavity on each arm and two rycycling optical cavities. The different feature of these detectors is the cryogenic test masses. To cool down to cryogenic, tipicaly 22 K, the test mass mirror is made of sapphire because of the high thermal conductivity and mechanichal Q value even in cryogenic environment. These properties can reduce some problems of the interferometeric GW detectors; thermal lens effect and thermal noise. The main interferometer is divided into four parts; (1) arm caivties, (2) input and output mode cleaners (IMC and OMC), (3) power resycling cavities (PRC), (4) and signal resycling cavities (SRC). The first, the arm cavities are composed of input test masses (ITMs) and end test masses (ETMs) with high reflectivity corresponding to a finesse of 1530 not to increase the internal cavity power. The second, while IMC is used for clean out the higher-order spatial mode and stabilizing the frequency of main input laser, OMC is used for clean out the unwanted higher-order spatial modes and frequency sideband of the output beam. The IMC is the triangle optical cavity which is made to stabilize the input laser frequency above 1 Hz. The OMC is the bow-tie cavity composed of four mirrors. The third, PRC is used for increasing the input laser power by 10 times. This cavity is composed of three mirrors named PRM, PR2 and PR3, respectively. The forth, SRC is used for expand the bandwidth of GW signals.This technique is more important than Advanced LIGO and Advanced Virgo, because the bandwidth is narrower than other detectors due to a high finesse arm cavity of KAGRA.

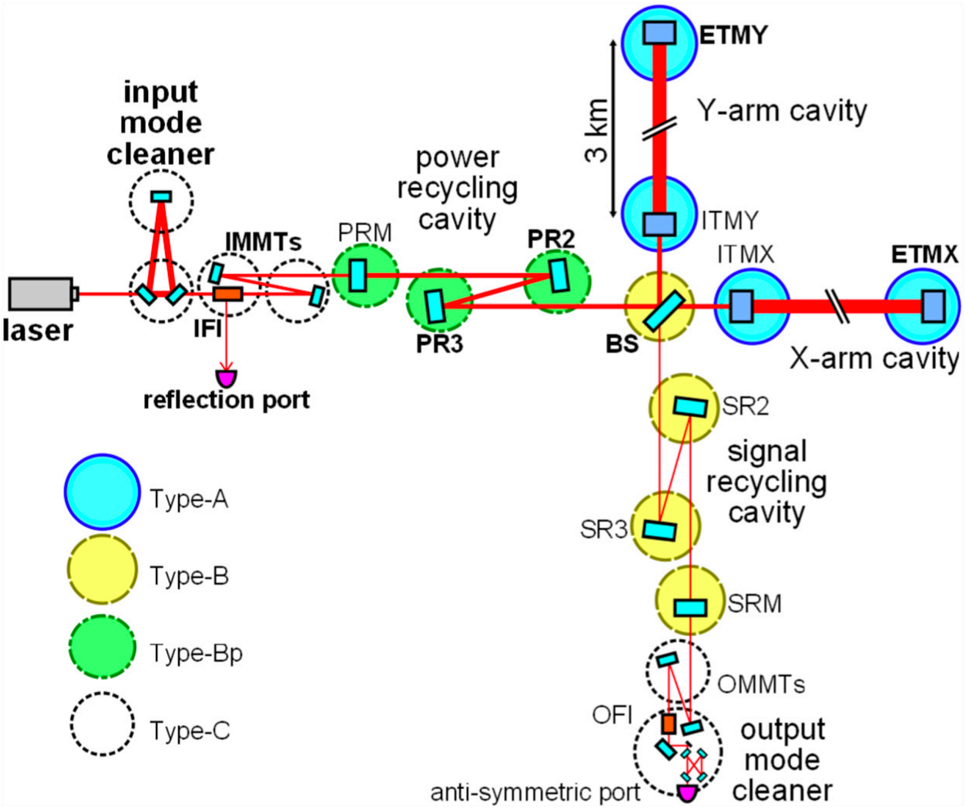

(a) Schematic interferometer configuration of KAGRA [82]

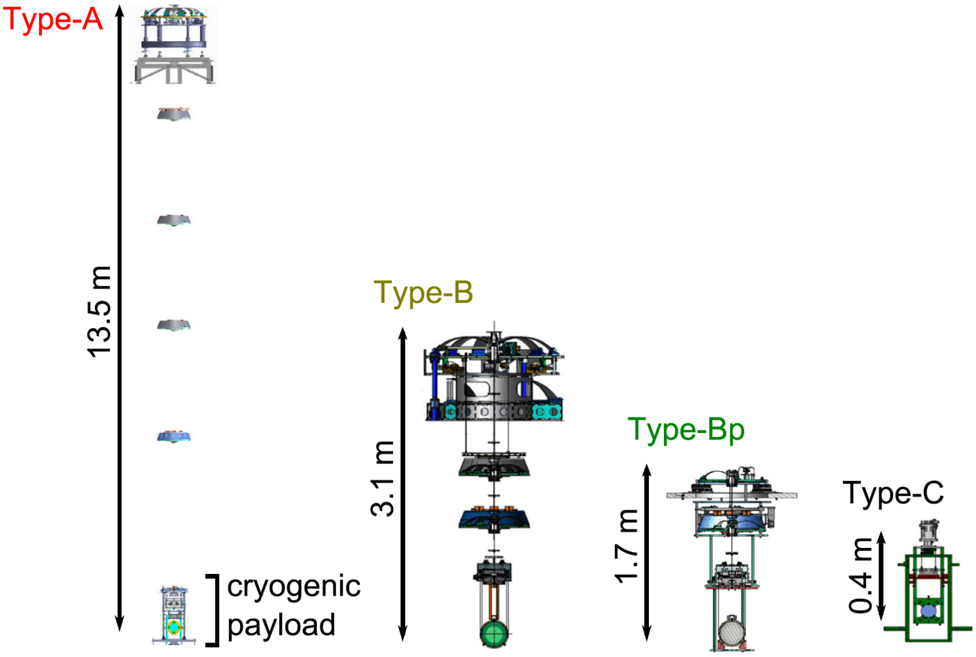

(b) KAGRA mirror suspension system [82]

Figure A.1: Interferometer configuration and mirror suspension system

A.1.3 Mirror Suspension System

All mirrors of the interferometer are suspended by four types suspensions; Type-A, Type-B, Type-Bp, Type-C. These suspensions are shown in Figure A.1b. The Type-A is a 13.5 m scale 9-stage pendulum suspending the test mass mirror. The Type-B is a small size of Type-A suspension for suspending the signal recycling mirrors and beam splitter mirror. The Type-Bp is also small size of Type-B but without the pre-isolator stage, which is for the power recycling mirrors. The type-C is the simple 2-stage suspension used in TAMA300 but with minor modification.

A.2 KAGRA Type-A Suspension

A.2.1 Overview

In order to suspend the cryogenic test mass, as shown in Fig.A.2, KAGRA Type-A suspension has two parts; cryogenic payload and 13.5 m room temperature tower pendulum [83]. The cryogenic payload is consisted of Platform, Marionette, Intermediate mass, Test mass. The tower is consited of 5 mechanical filter; Top filter, F1, F2, F3, and Bottom filter. Moreover, the suspension point of tower is suspended by pre-isolator stage which has a inverted pendulum.

In terms of the low-frequency seismic attenuation, the pre-isolator is the important mechanical part.

A.2.2 Pre-Isolator stage (PI)

The pre-isolator (PI) is a active seismic iolator for the suspension point of the long Type-A or Type-B suspensions. As shown in Figure A.3a, the suspension point is on the platform stage suported by the inverted pendlum (IP) which isolates the seismic noise in horizontal direction. For vertical direction, geometric anti-spring (GAS) suspends this point. Especially, horizontal motion of the platform stage is isolated by using the feedback control with the inertial sensor and the relative position sensor, which is described in the section ??.

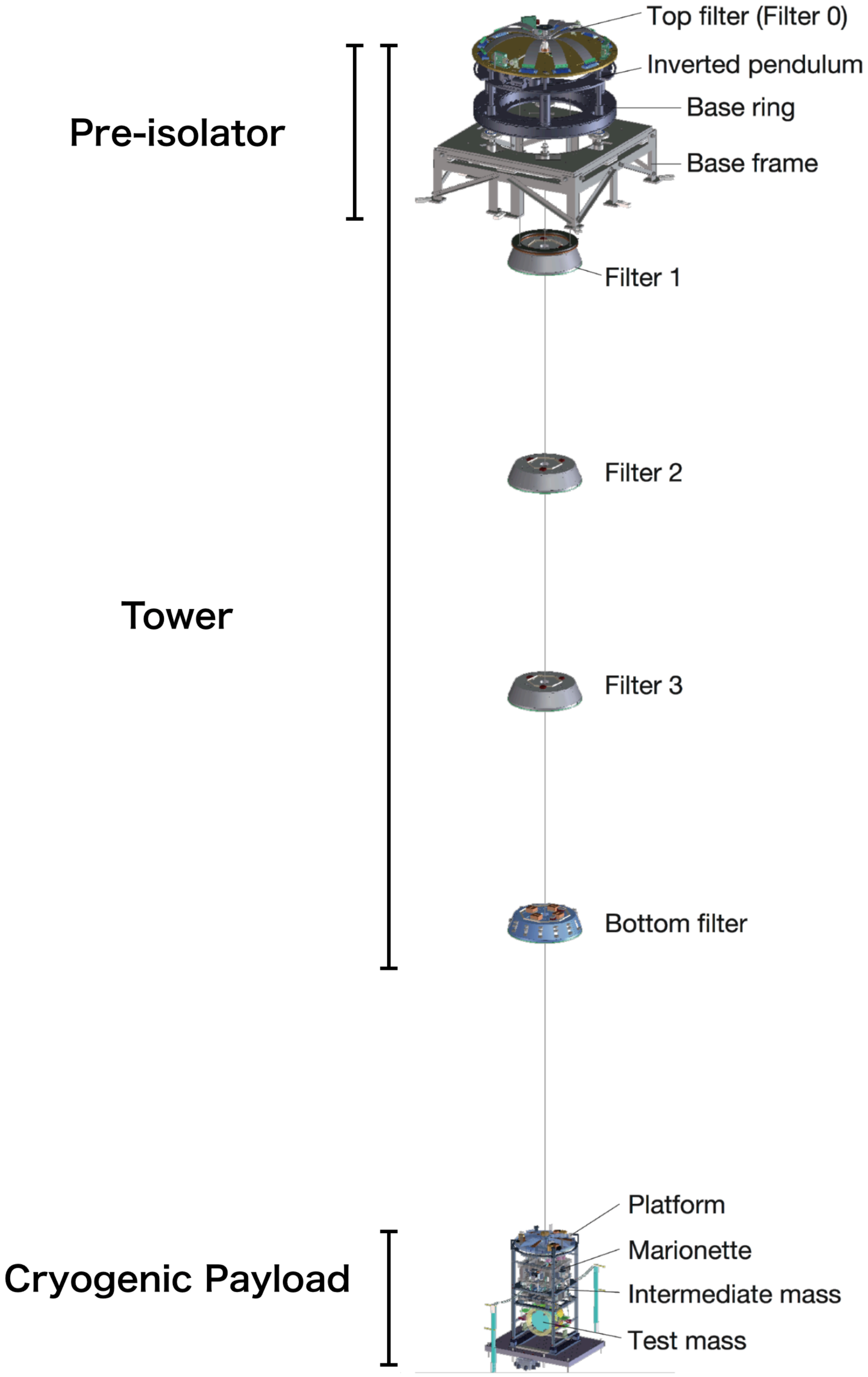

Figure A.2: An overview of the Type-A suspension [83]. Test mass is suspend by a 13.5 m pendulum consisted of several mechanichal filters. The suspension point of the long pendulum is suported by the pre-isolator, which consists of inverted pendulum, on the ground through the base frame and base ring.

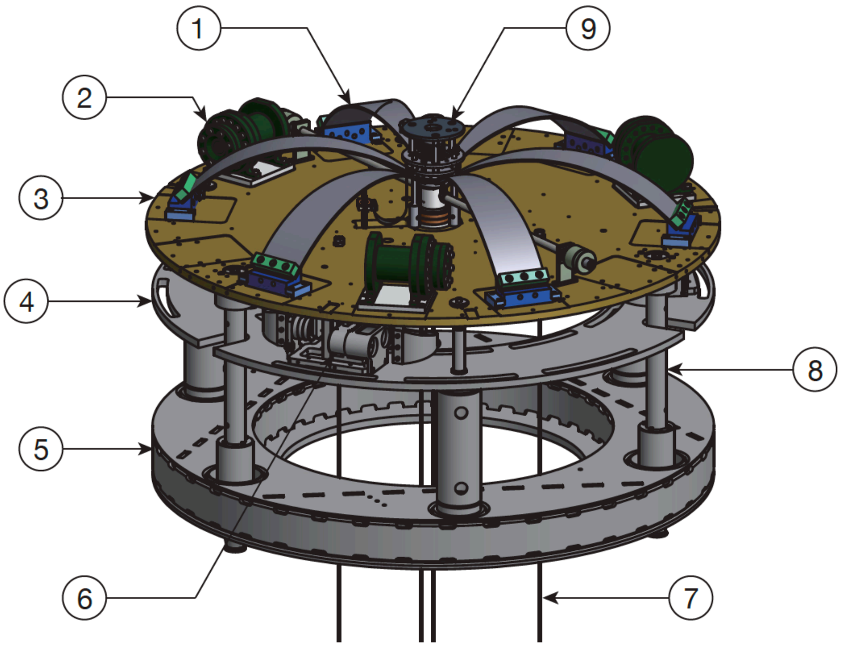

(a) Pre-isolator stage (PI). (1) Cantilever blade for GAS. (2) Geophone (3) Table of the top stage (4) Refernce frame rigidly connected to the base ring (5) The base ring mounted on the ground (6) LVDT and the coil magnet actuator (7) suspension wire to suspend the lower stages (8) leg of the inverted pendulum (IP). Figure is cited from figure 3.9 in [83]

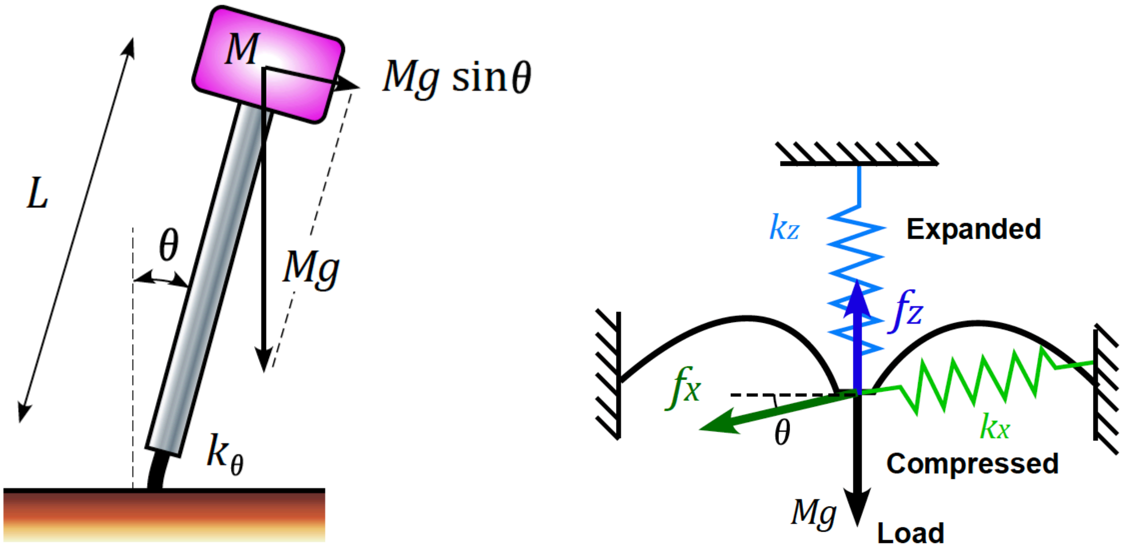

(b) Leg of the inverted pendulum (IP) [70].

(c) Geometrical Anti-Spring [70].

Figure A.3: CAD drawing of the pre-isolator (top) and main mechanical components of PI; IP leg and GAS (bottom).

Inverted pendulum for horizontal vibration isolation

Inverted pendulum (IP) is the low eigenfrequency pendulum because this mechanical filter can adjust the effective spring constant to small value by tuning the load on the platform stage. The angluar eigenfrequency of the singla IP leg is given by [70]

$$\omega_{\mathrm{IP}} = \sqrt{\frac{g}{L}\left(\frac{k_\theta/gL - M}{M}\right)}, \tag{A.1}$$

$$\tag{A.2}$$

where k_θ is the bending spring constant of the flexure, M is the mass of the stage and L is the length of the leg. Although the eigenfrequency ca be adjusted to zero in prônciple, actual eigenfrequency is designed at least 100 mHz because it is unstable when the term in square root is minus value.

Geometric Anti-Spring for vertical vibration isolation

Geometric anti-speing is also the low eigenfrequency pendlum in vertial direction. The eigenfrequency is adjusted to small value by compressing the cantilever blades as shown in Figure A.3c. The angular eigenfrequency is given by

$$\omega_{\mathrm{GAS}} = \sqrt{\frac{1}{M}\left[k_z - \left(\frac{l_0}{x_0} - 1\right)k_x\right]}, \tag{A.3}$$

where M is the load mass, k_{x} and k_{z} are the elastic constant of the compressed catilevers, l_0 is a natural length of the blades, x_0 is the horizontal distance between the central keystone and the support poit of the blades. One can find that the angular eigenfrequency of the GAS is reduced when $x_0 < l_0$.

Liner Variable Differential Transducer (LVDT)

LVDT is a wide range relative position sensor composed of three coils [84]. shown in Fig.A.4. The emitter coil is mounted on the pre-isolator stage and driven with a sinusoidal signal to emit a modulated magnetic field. The two receiver coils is mounted on the reference structure, and these coils are counter-wound to each other. When the emitter coil is on the center of two reciever coils, induced voltage is not emitted from the reciever coils. On the other hand, when the pre-isolater is moved, a sinusoidal signal apprears on the reciever coils. Therefore, after demodulating this signal, amplitude of output signal is propotional to the displacement from the LVDT geometrical center.

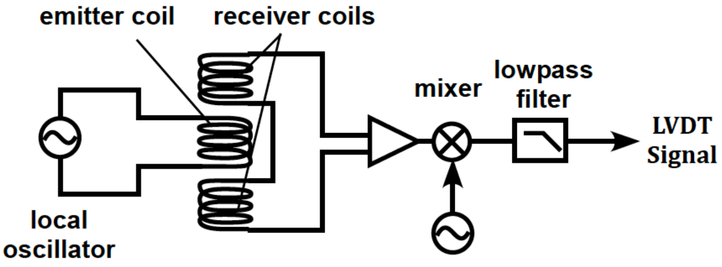

Figure A.4: [70]

Coil-magnet actuator

We use a voice-coil type wide range actuator to move the pre-isolator stage [85].

Bibliography

[1] Albert Einstein. The Foundation of the General Theory of Relativity. *Annalen Phys.*, 49(7):769–822, 1916. [Annalen Phys.354,no.7,769(1916)].

[2] Curt Cutler and Kip S Thorne. An overview of gravitational-wave sources. In *General Relativity and Gravitation*, pages 72–111. World Scientific, 2002.

[3] BP Abbott, R Abbott, TD Abbott, S Abraham, F Acernese, K Ackley, C Adams, RX Adhikari, VB Adya, C Affeldt, et al. Gwtc-1: a gravitational-wave transient catalog of compact binary mergers observed by ligo and virgo during the first and second observing runs. *Physical Review X*, 9(3):031040, 2019.

[4] Paola Leaci, LIGO Scientific Collaboration, Virgo Collaboration, et al. Searching for continuous gravitational wave signals using ligo and virgo detectors. In *Journal of Physics: Conference Series*, volume 354, page 012010. IOP Publishing, 2012.

[5] Mark Hereld. *A Search for Gravitational Radiation from PSR 1937+ 214*. PhD thesis, California Institute of Technology, 1984.

[6] Christian D Ott, Adam Burrows, Eli Livne, and Rolf Walder. Gravitational waves from axisymmetric, rotating stellar core collapse. *The Astrophysical Journal*, 600(2):834, 2004.

[7] AA Starobinskii. Spectrum of relict gravitational radiation and the early state of the universe. *JETP Letters*, 30:682–685, 1979.

[8] Nelson Christensen. Stochastic gravitational wave backgrounds. *Reports on Progress in Physics*, 82(1):016903, nov 2018.

[9] Alan H. Guth. Inflationary universe: A possible solution to the horizon and flatness problems. *Phys. Rev. D*, 23:347–356, Jan 1981.

[10] Rainer Weiss. Electronically coupled broadband gravitational antenna. 1972.

[11] Masaki Ando. *Power recycling for an interferometric gravitational wave detector.* PhD thesis, University of Tokyo, 1998.

[12] Brian J Meers. Recycling in laser-interferometric gravitational-wave detectors. *Physical Review D*, 38(8):2317, 1988.

[13] Jan Harms. Terrestrial gravity fluctuations. *Living reviews in relativity*, 18(1):3, 2015.

[14] Jennifer Clair Driggers. *Noise Cancellation for Gravitational Wave Detectors.* PhD thesis, California Institute of Technology, 2015.

[15] Dan Chen. *Study of a cryogenic suspension system for the gravitational wave telescope KAGRA.* PhD thesis, University of Tokyo, 2016.

[16] Yu. Levin. Internal thermal noise in the ligo test masses: A direct approach. *Phys. Rev. D*, 57:659–663, Jan 1998.

[17] Kenji Numata, Masaki Ando, Kazuhiro Yamamoto, Shigemi Otsuka, and Kimio Tsubono. Wide-band direct measurement of thermal fluctuations in an interferometer. *Phys. Rev. Lett.*, 91:260602, Dec 2003.

[18] Gregory M Harry, Andri M Gretarsson, Peter R Saulson, Scott E Kittelberger, Steven D Penn, William J Startin, Sheila Rowan, Martin M Fejer, DRM Crooks, Gianpietro Cagnoli, et al. Thermal noise in interferometric gravitational wave detectors due to dielectric optical coatings. *Classical and Quantum Gravity*, 19(5):897, 2002.

[19] Chiang-Mei Chen, James M Nester, and Wei-Tou Ni. A brief history of gravitational wave research. *Chinese Journal of Physics*, 55(1):142–169, 2017.

[20] Mark G. Beker. *Low-frequency sensitivity of next generation gravitational wave detectors.* PhD thesis, Vrije U., Amsterdam, 2013.

[21] 新藤 静夫. 武蔵野台地の地下地質. **地學雜誌**, 78(7):449–470, 1970.

[22] Shuichi Sato, Shinji Miyoki, Souichi Telada, Daisuke Tatsumi, Akito Araya, Masatake Ohashi, Yoji Totsuka, Mitsuhiro Fukushima, Masa-Katsu Fujimoto, LISM

Collaboration, et al. Ultrastable performance of an underground-based laser interferometer observatory for gravitational waves. *Physical Review D*, 69(10):102005, 2004.

[23] M Ohashi, K Kuroda, S Miyoki, T Uchiyama, K Yamamoto, K Kasahara, T Shintomi, A Yamamoto, T Haruyama, Y Saito, et al. Design and construction status of clio. *Classical and Quantum Gravity*, 20(17):S599, 2003.

[24] Masaki Ando, Koji Arai, Ryutaro Takahashi, Gerhard Heinzel, Seiji Kawamura, Daisuke Tatsumi, Nobuyuki Kanda, Hideyuki Tagoshi, Akito Araya, Hideki Asada, et al. Stable operation of a 300-m laser interferometer with sufficient sensitivity to detect gravitational-wave events within our galaxy. *Physical Review Letters*, 86(18):3950, 2001.

[25] Hartmut Grote, LIGO Scientific Collaboration, et al. The geo 600 status. *Classical and Quantum Gravity*, 27(8):084003, 2010.

[26] Hirotaka Takahashi, Hideyuki Tagoshi, Masaki Ando, Koji Arai, Peter Beyersdorf, Nobuyuki Kanda, Seiji Kawamura, Norikatsu Mio, Shinji Miyoki, Shigenori Moriwaki, et al. Coincidence analysis to search for inspiraling compact binaries using tama300 and lism data. *Physical Review D*, 70(4):042003, 2004.

[27] Stephen Fairhurst, Gianluca M. Guidi, Patrice Hello, John T. Whelan, and Graham Woan. Current status of gravitational wave observations. *General Relativity and Gravitation*, 43(2):387–407, Feb 2011.

[28] F Acernese, M Agathos, K Agatsuma, D Aisa, N Allemandou, A Allocca, J Amarni, P Astone, G Balestri, G Ballardin, et al. Advanced virgo: a second-generation interferometric gravitational wave detector. *Classical and Quantum Gravity*, 32(2):024001, 2014.

[29] Junaid Aasi, BP Abbott, Richard Abbott, Thomas Abbott, MR Abernathy, Kendall Ackley, Carl Adams, Thomas Adams, Paolo Addesso, RX Adhikari, et al. Advanced ligo. *Classical and quantum gravity*, 32(7):074001, 2015.

[30] B P Abbott, R Abbott, T D Abbott, M R Abernathy, K Ackley, C Adams, P Addesso, R X Adhikari, V B Adya, C Affeldt, et al. Exploring the sensitivity of next generation gravitational wave detectors. *Class. Quantum Grav*, 34(044001):044001, 2017.

[31] Takayuki Tomaru, Toshikazu Suzuki, Tomiyoshi Haruyama, Takakazu Shintomi, Nobuaki Sato, Akira Yamamoto, Yuki Ikushima, Tomohiro Koyama, and Rui Li. Development of a cryocooler vibration-reduction system for a cryogenic interferometric gravitational wave detector. *Classical and Quantum Gravity*, 21(5):S1005, 2004.

[32] Takashi Uchiyama, Shinji Miyoki, Souichi Telada, Kazuhiro Yamamoto, Masatake Ohashi, Kazuhiro Agatsuma, Koji Arai, Masa-Katsu Fujimoto, Tomiyoshi Haruyama, Seiji Kawamura, et al. Reduction of thermal fluctuations in a cryogenic laser interferometric gravitational wave detector. *Physical review letters*, 108(14):141101, 2012.

[33] Adam J Mullavey, Bram JJ Slagmolen, John Miller, Matthew Evans, Peter Fritschel, Daniel Sigg, Sam J Waldman, Daniel A Shaddock, and David E McClelland. Arm-length stabilisation for interferometric gravitational-wave detectors using frequency-doubled auxiliary lasers. *Optics express*, 20(1):81–89, 2012.

[34] Kiwamu Izumi. *Multi-Color Interferometry for Lock Acquisition of Laser Interferometric Gravitational-wave Detectors.* PhD thesis, University of Tokyo, 2012.

[35] S Biscans, J Warner, R Mittleman, C Buchanan, M Coughlin, M Evans, H Gabbard, J Harms, B Lantz, N Mukund, A Pele, C Pezerat, P Picart, H Radkins, and T Shaffer. Control strategy to limit duty cycle impact of earthquakes on the LIGO gravitational-wave detectors. *Classical and Quantum Gravity*, 35(5):055004, jan 2018.

[36] M Punturo, M Abernathy, F Acernese, B Allen, Nils Andersson, K Arun, F Barone, B Barr, M Barsuglia, M Beker, et al. The einstein telescope: a third-generation gravitational wave observatory. *Classical and Quantum Gravity*, 27(19):194002, 2010.

[37] L Naticchioni, M Perciballi, F Ricci, E Coccia, V Malvezzi, F Acernese, F Barone, G Giordano, R Romano, M Punturo, et al. Microseismic studies of an underground site for a new interferometric gravitational wave detector. *Classical and Quantum Gravity*, 31(10):105016, 2014.

[38] 西村太志 長谷川昭, 佐藤春夫. *Seismology*, volume 6 of *Introduction to Modern Erath Science Series.* Kyoritsu, 2015.

[39] 竹本修三, 新谷昌人, 赤松純平, 森井亙, 東敏博, 福田洋一, 尾上謙介, 市川信夫, 川崎一朗, 大橋正健, et al. 神岡鉱山における 100 メートルレーザー伸縮計について. **京都大学防災研究所年報**, 2003.

[40] Sylvette Bonnefoy-Claudet, Fabrice Cotton, and Pierre-Yves Bard. The nature of noise wavefield and its applications for site effects studies: A literature review. *Earth-Science Reviews*, 79(3-4):205–227, 2006.

[41] E J Daw, J A Giaime, D Lormand, M Lubinski, and J Zweizig. Long-term study of the seismic environment at LIGO. *Classical and Quantum Gravity*, 21(9):2255–2273, apr 2004.

[42] M G Beker, J F J van den Brand, E Hennes, and D S Rabeling. Newtonian noise and ambient ground motion for gravitational wave detectors. *Journal of Physics: Conference Series*, 363:012004, jun 2012.

[43] R. Schofield et al. Source and propagation of the predominant 1-50 hz seismic signal from off-site at ligo-hanford. In LIGO Scientific Collaboration Meeting, Hanford, August 2000.

[44] F Acernese, P Amico, N Arnaud, D Babusci, R Barillé, F Barone, L Barsotti, M Barsuglia, F Beauville, MA Bizouard, et al. Properties of seismic noise at the virgo site. *Classical and Quantum Gravity*, 21(5):S433, 2004.

[45] Jon R Peterson. Observations and modeling of seismic background noise. Technical report, US Geological Survey, 1993.

[46] Kiwamu Nishida, Naoki Kobayashi, and Yoshio Fukao. Origin of earth's ground noise from 2 to 20 mhz. *Geophysical Research Letters*, 29(10):52–1, 2002.

[47] P Bormann. New manual of seismological observatory practice. *GFZ German Research Centre for Geosciences*, 2012. Link.

[48] RA Haubrich, WH Munk, and FE Snodgrass. Comparative spectra of microseisms and swell. *Bulletin of the Seismological Society of America*, 53(1):27–37, 1963. Link.

[49] Michael Selwyn Longuet-Higgins. A theory of the origin of microseisms. *Philosophical Transactions of the Royal Society of London. Series A, Mathematical and Physical Sciences*, 243(857):1–35, 1950. Link.

[50] GG Sorrells, John A McDonald, ZA Der, and Eugene Herrin. Earth motion caused by local atmospheric pressure changes. *Geophysical Journal International*, 26(1-4):83–98, 1971.

[51] W Zürn and R Widmer. On noise reduction in vertical seismic records below 2 mhz using local barometric pressure. *Geophysical Research Letters*, 22(24):3537–3540, 1995.

[52] Duncan Carr Agnew. Earth tides: an introduction. 2005.

[53] Keiiti Aki and Paul G Richards. *Quantitative seismology.* 2002.

[54] Keiiti Aki. Scaling law of seismic spectrum. *Journal of geophysical research*, 72(4):1217–1231, 1967.

[55] B. Gutenberg. Amplitudes of surface waves and magnitudes of shallow earthquakes*. *Bulletin of the Seismological Society of America*, 35(1):3–12, 01 1945.

[56] Nanometrics Inc., 250 Herzberg Road Kanata, Ontario, Canada K2K 2A1. *Trillium 120Q/QA User Guide*, 04 2017.

[57] Rolf Bork, R Abbott, D Barker, and J Heefner. An overview of the ligo control and data acquisition system. *arXiv preprint physics/0111077*, 2001.

[58] A ARAYA. Broadband observation with laser strainmeters and a strategy for high resolution long-term strain observation based on quantum standard. *J. Geod. Soc. Japan*, 53:81–97, 2007.

[59] Akito Araya, Akiteru Takamori, Wataru Morii, Kouseki Miyo, Masatake Ohashi, Kazuhiro Hayama, Takashi Uchiyama, Shinji Miyoki, and Yoshio Saito. Design and operation of a 1500-m laser strainmeter installed at an underground site in kamioka, japan. *Earth, Planets and Space (Online)*, 69(1):1, 2017.

[60] Philip E Ciddor. Refractive index of air: new equations for the visible and near infrared. *Applied optics*, 35(9):1566–1573, 1996.

[61] Charlotte Bond, Daniel Brown, Andreas Freise, and Kenneth A Strain. Interferometer techniques for gravitational-wave detection. *Living reviews in relativity*, 19(1):3, 2016.

[62] Orazio Svelto. *Principles of lasers*, volume 4. Springer.

[63] Fritz Riehle. *Frequency standards: basics and applications*. John Wiley & Sons, 2006.

[64] Kouseki Miyo. 重力波望遠鏡 kagra のための地殻変動モニターの開発. Master's thesis, University of Tokyo, 2017.

[65] Akito Araya, Takashi Kunugi, Yoshio Fukao, Isao Yamada, Naoki Suda, Sumitaka Maruyama, Norikatsu Mio, and Shigenori Moriwaki. Iodine-stabilized nd: Yag laser applied to a long-baseline interferometer for wideband earth strain observations. *Review of scientific instruments*, 73(6):2434–2439, 2002.

[66] James J Snyder, Rama K Raj, Daniel Bloch, and Martial Ducloy. High-sensitivity nonlinear spectroscopy using a frequency-offset pump. *Optics letters*, 5(4):163–165, 1980.

[67] Norman Bobroff. Recent advances in displacement measuring interferometry. *Measurement Science and Technology*, 4(9):907, 1993.

[68] Mark A Zumberge, Jonathan Berger, Matthew A Dzieciuch, and Robert L Parker. Resolving quadrature fringes in real time. *Applied optics*, 43(4):771–775, 2004.

[69] Takanori Sekiguchi. *A Study of Low Frequency Vibration Isolation System for Large Scale Gravitational Wave Detectors*. PhD thesis, Department of Physics School of Science, University of Tokyo, 2016.

[70] F Matichard, B Lantz, R Mittleman, K Mason, J Kissel, B Abbott, S Biscans, J McIver, R Abbott, S Abbott, et al. Seismic isolation of advanced ligo: Review of strategy, instrumentation and performance. *Classical and Quantum Gravity*, 32(18):185003, 2015.

[71] Wensheng Hua. *LOW FREQUENCY VIBRATION ISOLATION AND ALIGNMENT SYSTEM FOR ADVANCED LIGO*. PhD thesis, stanford university, 2005.

[72] Christophe Collette, Stefan Janssens, Pablo Fernandez-Carmona, Kurt Artoos, Michael Guinchard, Claude Hauviller, and André Preumont. Inertial sensors for low-frequency seismic vibration measurement. *Bulletin of the seismological society of America*, 102(4):1289–1300, 2012.

[73] Sebastein Biscans. *Optimization of the Advanced LIGO gravitational-wave detectors duty cycle by reduction of parametric instabilities and environmental impacts.* PhD thesis, University of Maine, 2018.

[74] R. W. P . Drever. Outline of a proposed design for a first receiver for installation in the long-baseline facilities, of fabry-perot type. Technical Report T870001-00-R, LIGO Document, 9 1987.

[75] Ronald WP Drever and Steven J Augst. Extension of gravity-wave interferometer operation to low frequencies. *Classical and Quantum Gravity*, 19(7):2005, 2002.

[76] Y Aso, M Ando, K Kawabe, S Otsuka, and K Tsubono. Stabilization of a fabry–perot interferometer using a suspension-point interferometer. *Physics Letters A*, 327(1):1–8, 2004.

[77] Kenji Numata and Jordan Camp. Interferometric testbed for nanometer level stabilization of environmental motion over long time scales. *Appl. Opt.*, 47(36):6832–6841, Dec 2008.

[78] Yuta Michimura, Tomofumi Shimoda, Takahiro Miyamoto, Ayaka Shoda, Koki Okutomi, Yoshinori Fujii, Hiroki Tanaka, Mark A Barton, Ryutaro Takahashi, Yoichi Aso, et al. Mirror actuation design for the interferometer control of the kagra gravitational wave telescope. *Classical and Quantum Gravity*, 34(22):225001, 2017.

[79] J Aasi, J Abadie, BP Abbott, Robert Abbott, T Abbott, MR Abernathy, T Accadia, F Acernese, C Adams, T Adams, et al. Characterization of the ligo detectors during their sixth science run. *Classical and Quantum Gravity*, 32(11):115012, 2015.

[80] RWP Drever, John L Hall, FV Kowalski, J_ Hough, GM Ford, AJ Munley, and H Ward. Laser phase and frequency stabilization using an optical resonator. *Applied Physics B*, 31(2):97–105, 1983.

[81] T Akutsu, M Ando, K Arai, Y Arai, S Araki, A Araya, N Aritomi, H Asada, Y Aso, S Atsuta, et al. First cryogenic test operation of underground km-scale gravitational-wave observatory kagra. *arXiv preprint arXiv:1901.03569*, 2019.

[82] Okutomi Koki. *Development of 13.5-meter-tall Vibration Isolation System for the Main Mirrors in KAGRA*. PhD thesis, SOKENDAI, The Graduate University for Advanced Studies, 2019. Link.

[83] Hareem Tariq et al. The linear variable differential transformer (LVDT) position sensor for gravitational wave interferometer low-frequency controls. *Nucl. Instrum. Meth.*, A489:570–576, 2002.

[84] Chenyang Wang, Hareem Tariq, Riccardo DeSalvo, Yukiyoshi Iida, Szabolcs Marka, Yuhiko Nishi, Virginio Sannibale, and Akiteru Takamori. Constant force actuator for gravitational wave detector's seismic attenuation systems (sas). *Nuclear Instruments and Methods in Physics Research Section A: Accelerators, Spectrometers, Detectors and Associated Equipment*, 489(1-3):563–569, 2002.